TÉCNICO LISBOA

Planar Antennas for CubeSat Missions

Tomás Alexandre Saltão Almeida

Thesis to obtain the Master of Science Degree in

Electronics Engineering

Supervisors: Prof. Carlos António Cardoso Fernandes
Prof. Jorge Manuel Lopes Leal Rodrigues da Costa

Examination Committee

Chairperson: Prof. Pedro Miguel Pinto Ramos
Supervisor: Prof. Carlos António Cardoso Fernandes
Members of the Committee: Prof. Marco Alexandre dos Santos Ribeiro

November 2018

Acknowledgments

First and foremost, I want to thank my supervisor, Professor Carlos Fernandes, for his excellent guidance and support, and for always pushing me to achieve more and trying out new ideas to solve the barriers encountered during the development of this thesis.

I would like to thank António Almeida for his invaluable help during this whole thesis, including the build of prototypes, measurements, and advice. Also, special thanks go to Mr. Carlos Brito and Mr. Farinha, for the fabrication of the multiple prototypes. I want also to thank PhD student João Felício, for his invaluable help and advice.

I am also very grateful for the support from Instituto de Telecomunicações, for financing the material used in this thesis, and also for the usage of their laboratories, both for fabrication and measurements.

Very special thanks go to my loved ones, for believing in me and pushing me to always achieve the best, and for the special support during this long period.

Abstract

CubeSats are a type of pico-satellites that have a standardized size of 10 x 10 x 10 cm^3 (1U), or 1U multiples, and weigh less than 1.33 kg per cubic unit. A few challenges arise when designing an antenna to be integrated in the CubeSat's small structure. Miniaturization techniques must be used to shrink antenna size and deployable antennas solutions can be used when bigger antenna apertures are needed e.g., in applications that require a high gain antenna. Also, special challenges arise due to the harsh environment in space.

In this thesis, two different planar antennas for CubeSat applications are designed and fabricated. First, a patch antenna for the ISTsat-1 CubeSat, is developed. Secondly, a reflect array (RA) antenna is developed for a possible ISTsat-2 mission. The antenna for ISTsat-1 operates in the L band, more specifically 1090 MHz, and is for an automatic dependent surveillance – broadcast mission (ADS-B). The second antenna operates in the Ka uplink band of 27 - 31 GHz, and can be used for multiple applications, e.g. fast mobile broadband access.

During the development of the antennas in this thesis, simulation studies are performed, as well as the fabrication of prototypes, and specific experimental tests. In regard to the ISTsat-1 ADS-B antenna, a fully functional, flight ready antenna, is presented.

Keywords

CubeSat, ISTsat-1, Satellite Antennas, Planar Antennas, Patch Antenna, Reflect Array

Resumo

CubeSats são um tipo de pico-satélites com um tamanho padrão de 10 x 10 x 10 cm^3 (1U), ou múltiplos de 1U, pesando menos de 1.33 kg por unidade cúbica. Surgem alguns problemas quando se desenha uma antena para ser integrada na pequena estrutura de um CubeSat. Técnicas de miniaturização são precisas para diminuir o tamanho físico da antena, sendo que soluções de antenas desdobráveis podem ser usadas quando antenas de elevada abertura são necessárias, por exemplo em missões que requerem antenas de ganho elevado. Aparecem também desafios especiais devido ao ambiente severo que é o espaço.

Nesta tese, duas antenas planares diferentes, para aplicações em CubeSats são desenhadas e fabricadas. Primeiro uma antena tipo *patch* para o CubeSat ISTsat-1 é desenvolvida. Segundo, uma antena *reflect array* (RA) é desenvolvida, para uma possível missão de um ISTsat-2. A antena para o ISTsat-1 opera na banda L, mais especificamente a 1090 MHz, e vai ser usada para uma missão de *automatic dependent surveillance – broadcast* (ADS-B). A segunda antena opera na banda Ka de *uplink* (27 - 31 GHz) e pode ser usada em inúmeras aplicações, uma delas banda larga móvel de alta velocidade.

Durante o desenvolvimento das antenas presentes nesta tese, são realizados estudos por simulação, o fabrico de protótipos e testes experimentais específicos. Em relação à antena de ADS-B do ISTsat-1, uma antena na versão final (*flight ready*), é apresentada.

Palavras Chave

CubeSat, ISTsat-1, Antenas para Satélites, Antenas Planares, Antenas *Patch*, Antenas *Reflect Array*

Contents

List of Figures

List of Tables

Acronyms

ADS-B	Automatic Dependent Surveillance – Broadcast
AUT	Antenna Under Test
Cal Poly	California Polytechnic State University
CST-MWS	Computer Simulation Technology - Microwave Studio
EM	Electromagnetic
ESA	European Space Agency
ESD	Electrostatic Discharge
FSS	Frequency-Selective Surface
GPS	Global Positioning System
HTS	High Throughput Satellites
IST	Instituto Superior Técnico
IT	Instituto de Telecomunicações
PCB	Printed Circuit Board
RA	Reflect Array
RF	Radio Frequency
SRRs	Split Ring Resonators
TA	Transmit Array
TTC	Telemetry, Tracking and Command
UHF	Ultra High Frequency

VHF Very High Frequency

VLSI Very Large Scale Integration

VNA Vector Network Analyzer

1

Introduction

Contents

Introduction

1.1 Purpose and Motivation

Nowadays, thousands of satellites are orbiting the Earth. We rely on many services that are assured by satellites, for example the Global Positioning System (GPS), satellite television, mobile broadband access, and weather monitoring. The design and construction of these conventional satellites is very costly and usually takes years from the developing phase to the launch phase.

With the miniaturization of electronics it is now possible to develop complex, low-power systems with small footprints. This technological push combined with the need to develop less expensive satellites led to the emergence of smaller satellites. These smaller satellites have limitations compared to conventional large satellites but are still suitable for certain missions.

CubeSats fit in this group of small satellites, and given their small size and low cost they are perfect for students or small companies that want to perform space research and testing of ideas that could, in the future, be implemented on larger service providing satellites.

An important component of a satellite is the antenna. In a satellite, antennas are used for Telemetry, Tracking and Command (TTC) which includes both downlink and uplink, for the payload and for inter-satellite communication. The payload antenna design depends on the mission the satellite is going to perform.

Expected to be launched in 2019, ISTsat-1 is a 1U (10 x 10 x 10 cm^3) CubeSat being developed by students of Instituto Superior Técnico (IST). Many universities want to join the space race, for exploration and research, and are spending a lot of resources in this field. IST is one of these universities and ISTsat-1 is one of the few satellites that got a chance to be launched to space, with the "Fly Your Satellite" program, supported by the European Space Agency (ESA). The satellite's main mission is to monitor airplanes using Automatic Dependent Surveillance – Broadcast (ADS-B) signals. Satellite ADS-B is a surveillance technology that enables the tracking of aircrafts in remote areas of the globe, where terrestrial ADS-B and radar technologies have no coverage. In this mission, there is something that will affect the communication between the aircrafts and the satellite, called the Cone of Silence, which is the region around the aircraft's zenith where, due to the aircraft antenna's radiation pattern, the coverage is very low, or non existent. With this in mind, it is also intended to characterize the Cone of Silence when the aircraft is at the satellite's nadir. To receive the ADS-B signals and guarantee a good communication link, a compact ADS-B antenna, that fits into the small CubeSat structure, had to be developed. The ADS-B antenna developed in this thesis is one of the satellite's subsystems developed in house. The other subsystems include an electric power system, an on-board computer, a communications processor, the ADS-B radio, and the TTC radio and respective Very High Frequency (VHF) and Ultra High Frequency (UHF) antennas, being the TTC antennas, commercial solutions.

In this thesis, two different antennas for CubeSats are developed. One antenna (for the sub 2 GHz band) for ISTsat-1, planned to be launched by ESA in 2019, and another for a future CubeSat mission (for the millimeter-wave band).

In inter-satellite communications, antennas with high-gain and high operation frequency are usually required to guarantee high-speed communication links. This is also true for High Throughput Satellites (HTS), whose main application is faster mobile broadband access. This thesis also presents a solution for an antenna that works in high frequency (Ka band), capable of being integrated in the CubeSat's structure, designed for HTS applications.

There are many challenges when designing an antenna for CubeSat platforms. One is the limited space available to integrate the antenna and the degradation of performance that comes with it. For some cases, antenna miniaturization techniques are required and for others, deployable antennas is the only option to fit larger antenna systems into the CubeSat's small structure. For the ISTsat-1 ADS-B antenna there are extra challenges such as, strict bandwidth requirements, resonance frequency variation with temperature, high efficiency requirement, influence of the satellite structure and V/UHF antennas, on the antenna's polarization and radiation pattern. In addition, that it has to be made on a material that can withstand vibrations, that has low outgassing properties, and is temperature stable. For the Ka band antenna, the main challenge is obtaining good antenna performance, in terms of gain, with a compact antenna system that fits into the 1U CubeSat. These stringent requirements make the design of good performing antennas very challenging.

1.2 Goals

This thesis is divided in two parts. A first part where an ADS-B patch antenna for ISTsat-1 is designed and fabricated, and a second part where a millimeter wave antenna is developed for a possible second mission with an ISTsat-2.

Regarding ISTsat-1's ADS-B antenna, one goal is to identify the antenna's requirements, by analyzing the mission objectives and limitations. The antenna is designed considering the following mission characteristics, link budget, ADS-B operational frequency and minimum bandwidth, and thermal noise. The antenna also needs to conform with the mission restrictions as, the available volume in the CubeSat, and the operational temperature that the antenna will experience in orbit. Considering the ISTsat-1's mission, its requirements and limitations, the best antenna solution is identified and fabricated.

For the Ka band antenna, the goal is to develop an antenna solution that is small enough to fit in a 1U CubeSat, has a high gain (>23 dB), and wide bandwidth, ideally to cover the entire Ka uplink band (27 GHz to 31 GHz).

1.3 Methodology

1.3.1 Project Methodology

Antenna design is an iterative process that has two main phases. One phase, where the antenna is designed and simulated using a 3D numerical Electromagnetic (EM) solver and a second phase where the prototype is built and tested in a Radio Frequency (RF) laboratory.

In this thesis, Computer Simulation Technology - Microwave Studio (CST-MWS) [1] is used to perform the modeling and 3D EM simulation of the antennas. The fabrication is done at IST and the measurements at Instituto de Telecomunicações (IT) RF laboratories in Lisbon. It is depicted in Figure 1.1, the general process of developing an antenna.

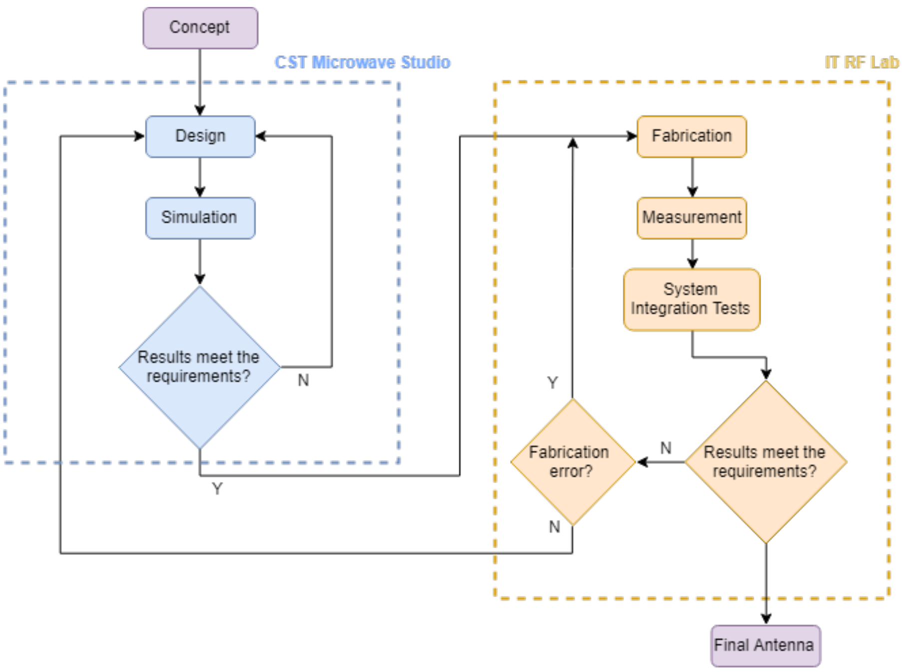

Figure 1.1: Methodology flow chart.

1.3.2 Test Methodology

Although having its complexities, the antenna for ISTsat-1 has to be of simple design in order to be easily integrated in the 1U CubeSat, but in the Ka band antenna, more strict design details have to be accounted for and they are studied in section 2.3. In this thesis, the measurement and test phase involves some extra steps to ensure good performance of the antennas.

Material Permittivity Test

Due to uncertainty on the electrical permittivity value, of the substrate materials used for the planar antennas in this thesis, in-house permittivity tests are performed to characterize their complex permittivity. For the ISTsat-1 antenna this is important because small shifts in the substrate's permittivity could translate into critical resonant shifts on the antenna's performance, due to the small bandwidth. This is also important for the Ka band antenna, but these tests will not be used as that antenna has more relaxed requirements in terms of bandwidth.

Impedance Test

The antenna's input impedance and correspondent S_{11} values, as a function of frequency, are measured with a Vector Network Analyzer (VNA), in order to evaluate the antenna's resonance within the band of interest. Also, it is important to test the antenna's input impedance under different temperatures, because in the harsh space environment, satellites suffer large temperature variations. Related to the impedance and the substrate losses, the antenna's efficiency is measured using the Wheeler cap method [2].

Radiation Pattern Test

The radiation pattern measurement for the ISTsat-1 antenna, is done at IT-IST chamber one, which is an 8.5 m x 4.5 m x 3.6 m anechoic chamber that has a frequency range from 1.8 GHz to 18 GHz. Since the ADS-B band is centered at 1.09 GHz and thus outside of the anechoic chamber's designed frequency band, higher discrepancy between simulations and measurements is expected. For the Ka band antenna, it is used IT-IST's chamber number two, which is an 4 m $\times$ 2.5 m $\times$ 2.4 m anechoic chamber that has a frequency range from 8 GHz to 110 GHz.

Integration with CubeSat Test

The input impedance at room temperature, and radiation pattern measurements are repeated with the CubeSat attached, and afterwards with the VHF and UHF antennas installed to analyze their influence.

ADS-B System Test

Specifically for the ISTsat-1 ADS-B antenna, preliminary tests with a commercial ADS-B receiver are performed, to see how the fabricated antenna performs as part of a complete ADS-B system, by analyzing the signals received from passing airplanes.

1.4 Document Structure

This document is organized as follows:

- Chapter 1 gives a brief overview of the topic, the goals of this thesis and the methodology taken for the antenna development.
- In chapter 2 it is presented the state of the art regarding small satellites and some types of antennas that stand as good solutions for CubeSat missions.
- In chapter 3 the mission requirements relevant to ISTsat-1's antenna, are presented. Also, the antenna is defined and its respective simulation and measured results, presented.
- Chapter 4 presents the design process and fabricated antenna solution, for the Ka band antenna.
- Finally, in chapter 5 a brief summary of the work developed in this thesis is presented, as well as considerations for future work related to this thesis.

2

State of the Art

Contents

State of the Art

2.1 Small Satellites

With the appearance of Very Large Scale Integration (VLSI) in the 1970's, it was then possible to include many discrete electronic components in one integrated circuit, thus reducing the overall size of the system as well as the weight and power consumption. This technological advance enabled the possibility of building smaller satellites using more compact electronic systems which in turn made the fabrication of such satellites cheaper, compared with the conventional satellites [3].

In attempt to demonstrate the feasibility of such smaller, low cost satellites, University of Surrey developed the UoSAT-1. The micro-satellite, launched in 1981, was designed and built by students and professors. The mission was a success and the satellite orbit lifetime was 8 years [4].

Modern small satellites can be divided in different groups based on their mass. Table 2.1 shows this categorization of satellites, from the big conventional satellites to the femto-satellites only weighing around 100 grams.

Table 2.1: Satellite categories based on mass, with correspondent average cost and proposal to launch times. Satellites are denoted as small, from mini to fempto classification [5].

Type	Mass (kg)	Cost (€)	Time of Development from Proposal to Launch
Conventional large satellite	>1000	90 - 1700 M	>5 years
Medium satellite	500-1000	45 - 90 M	4 years
Mini-satellite	100-500	9-45 M	3 years
Micro-satellite	10-100	1.7-9 M	∼1 year
Nano-satellite	1-10	0.17-1.7 M	∼1 year
Pico-satellite	<1	17-170k	<1 year
Femto-satellite	<0.1	0.1-17 k	<1 year

It can be seen that, as the mass of the satellite decreases its inherent cost and develop time, decrease as well. It is now possible, with these new types of satellites, to build a satellite in under one year and for a few thousand euros. The lower cost and faster develop times unlocked the usage of space for academic purposes where the money to invest on such projects is nowhere near as the one available in national and international space agencies. Although not as capable as conventional larger satellites, small satellites are very capable of performing specific missions. Also, extended functionalities can be achieved when many small satellites are used to form a satellite network.

As stated in chapter 1, antennas are a key component of all satellites. There are some challenges when designing an antenna for space applications and, on top of that, there are extra ones when designing an antenna for small satellites compared to larger ones. These challenges include [5]:

- Antennas should be small in size, due to the small available space to mount them.
- Antennas should be mechanically robust since the satellites experience high g-forces and vibrations upon launch.
- Antennas have to be designed to withstand the high temperature variations experienced in space. As an example, the CubeSat GOMX-1 at sun synchronous orbit, experiences an external temperature variation of -40 to 50 °C [6].
- Antennas must be able to handle space radiation, such as plasmas (especially at higher latitudes) and solar energetic particles. With this in mind, antennas should have an Electrostatic Discharge (ESD) mechanism.
- Antenna design and simulation should have in consideration the satellite's structure. The satellite's structure can cause EM scattering as well as degradation of the antenna's radiation pattern and gain.

The small available space to mount the antennas in the small satellites is a challenge that has two main solutions. First, a deployable antenna system can be integrated instead of a fixed one. When possible, the realization of deployable antennas for small satellites provide solutions where the antenna performs well and is insensitive to the deployment mechanism. This solution has the drawback of being dependent of a mechanical system, as the antenna's performance can be affected by the failure of the mechanical deployment system. The deployment may also consume considerable amounts of energy, and these systems usually occupy extra space, for the mechanical part of the deployer. If a fixed antenna solution is chosen, miniaturization techniques have to be applied in order to fit the antenna into the small satellite. This miniaturization, although good for reducing the antenna's physical size, has the disadvantage of affecting the antenna's performance e.g., in regards of antenna gain and efficiency.

2.1.1 CubeSats

CubeSats are a type of pico-satellites that were standardized with a collaboration between California Polytechnic State University (Cal Poly) and Stanford University. The purpose of this CubeSat project was to provide a standard for the design of pico-satellites, making the development of such satellites much cheaper and less time consuming compared with bigger satellites [7].

As the name implies, CubeSats are cubic satellites that have a dimension of 1U, which corresponds to 10 x 10 x 10 cm^3, and a mass under 1.33 kg. These structural specifications were made so that the CubeSats would fit in standardized deployers and be deployed smoothly. It is shown in figure 2.1 an assembled 1U CubeSat.

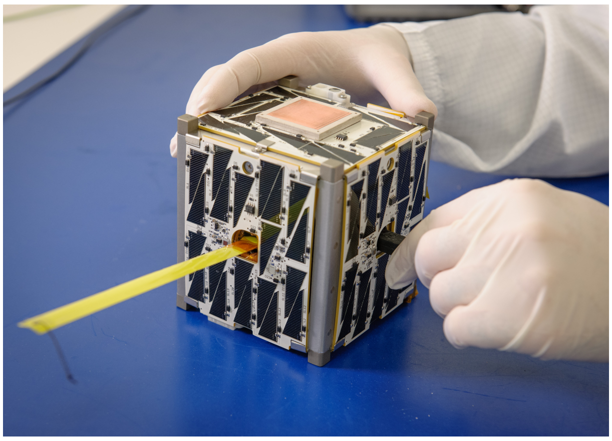

Figure 2.1: Phonesat 2.5, an 1U CubeSat built by NASA [8].

The rest of the satellite, meaning the hardware for the on-board computer, power control systems and payload, are dependent on what type of mission the satellite is going to preform. Nowadays, CubeSats can be built with different sizes, namely 1U multiples like the 3U, 6U and 12U CubeSats. The choice of the structure size is dependent on the mission, because different missions require different payloads and possibly different power requirements have to be met. The power on CubeSats normally comes from solar panels and if more power is required more surface area of panels is required, increasing the structure size.

As stated in chapter 1, CubeSats although small in size are the perfect tool for certain space missions. Some examples of missions carried out by CubeSats are:

- Earth observation, as in the case of storm monitoring and prediction, tested on the MicroMAS CubeSat [9].
- Space research. ExoplanetSat was developed so it can find transiting exoplanets by observing slight changes in light emanating from the planet's parent star [10].
- Inter-satellite communication, using CubeSats as nodes to relay messages within satellite constellations [11].

Different missions require different payload systems. If the payload has an antenna, different antennas have to be designed depending on what mission the satellite is going to preform. In sections 2.2

and 2.3, an overview of possible antenna designs for low frequency (sub 2 GHz) and high frequency (millimeter waves) is presented.

2.2 Sub 2 GHz Antennas

This section presents an overview of the different types of antennas that can be designed to work with operation frequencies bellow 2 GHz. The study of possible antenna solutions for this frequency band is important because the relevant ADS-B band is centered at 1090 MHz and thus fit in this category. ISTsat-1's TTC antennas operate at VHF and UHF bands, so they also belong to this group.

2.2.1 Monopoles and Dipoles

Consisting of only one or two thin wires, monopoles and dipoles are the simplest types of antennas that can be designed. A popular configuration is the half-wavelength dipole, where its physical length is half of a wavelength at resonant frequency. The length of such dipole, L, can be calculated as

$$L = \frac{c_0}{2f_r}, \tag{2.1}$$

where c_0 is the speed of light in vacuum and f_r the resonance frequency.

Dipoles can be considered as current radiators, because it is their oscillating current distribution that generates the propagated EM waves. That current distribution originates a omni-directional radiation pattern (constant in ϕ), that is null for $\theta = 0°, 180°$ and maximum for $\theta = 45°$, such radiation pattern is depicted in figure 2.2.

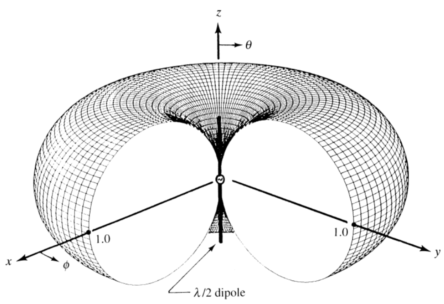

Figure 2.2: 3D radiation pattern of an half-wave dipole antenna [12].

In the case of the monopole, it also has an omni-directional radiation pattern but, since it is half of a dipole with a big ground plane underneath it only needs half the power to radiate.

Since the beginning of space exploration, monopoles and dipoles have been used for satellite communication, due to their broad omni-directional radiation pattern. The low directivity of these antennas is an advantage when the satellite does not have complex attitude control systems implemented, in the case that it enables more ground stations to be covered by the antennas.

Within the CubeSat topic, monopoles and dipoles are also a good antenna solution for some types of communication links. Challenges arise when working with smaller CubeSat structures, like the 1U CubeSat. Due to the antenna's large form factor for low operating frequencies (L band and bellow) they have to be deployable.

The deployability of these antennas can be realized in two ways. First, with the use of motors a folded or rolled antenna can be deployed when in orbit. The proposed antenna [13] for VHF operation uses this deployment method. The antenna is rolled in the stowed state and straight in the deployed state. It is reinforced with glass fiber epoxy in order to become elastically stable, both at stowed and deployed states, which means that no force is needed to maintain the stowed or deployed states, needing only an mechanical actuator to start the deployment. Second, a wire antenna made from a flexible conductive material can be folded and stowed inside the CubeSat's structure in a way that it stores strain energy. The antenna is secured with a wire and is released in orbit, regaining its original shape.

The wire that holds and releases the antennas is usually a nichrome burn wire [14], that heats up when supplied with a current, cutting a string of fiber that is holding the antenna. This deployment mechanism, although widely used in CubeSat missions, has the disadvantage of being prone to mechanical failure, as the wire can break from the heavy vibrations and forces experienced at launch. If the deployment mechanism fails, the antenna will not deploy and it would be almost impossible to achieve a communication link with the satellite. This problem was experienced by engineers at Cal Poly on their 3U CubeSat, the ExoCube [15].

2.2.2 Helical Antennas

An helical antenna consists of a conducting metal wire that is wound up in an helical shape, with a ground plane in the feeding edge. The antenna is fed through the bottom, with a coaxial cable for example. Figure 2.3 illustrates an helical antenna with ground plane. Some of the main design parameters of an helical antenna are, the turn diameter D, the turn circumference C, the vertical spacing between turns S and the pitch angle α. Helical antennas can be designed to radiate in many different modes, the most popular one being the end-fire. As an end-fire radiator, the helical antenna exhibits high gain with a maximum of radiation towards the +z direction. Due to its physical nature, circular polarization is easy to achieve in helical antennas and the more turns the antenna has the better the purity will be.

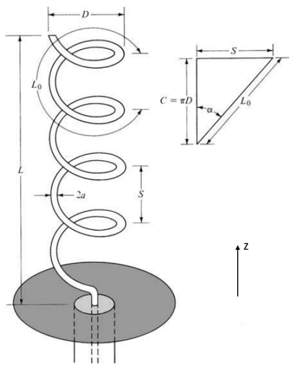

Figure 2.3: Helical antenna with ground plane underneath [12].

Due to their high gain, wide bandwidth and easiness of achieving circular polarization, the helical antennas stand as a good solution for satellite applications. Also, being the gain given by

$$\frac{6.2C^2NS}{{\lambda_0}^3}, \tag{2.2}$$

where N is the number of turns in the helix, λ_0 the resonant frequency and C, S defined above, another advantage is that to increase the gain one can increase the antenna's area in terms of C,N or S without affecting the occupied space in the satellite, meaning that it has a small footprint.

In order to achieve optimal circular polarization, the circumference of the helix must be in the $3\lambda_0/4\pi < D < 4\lambda_0/3\pi$ range and the spacing about $S \simeq \lambda_0/4$ [12]. This means that for 1 GHz of operating frequency, the helical antenna would have $D \simeq 7.16$ cm and $L \simeq 37.5$ cm for $N = 5$, being L the length of the helix. With this in mind, helical antennas integrated in CubeSats are usually of the deployable type, due to the size restrictions of the CubeSat standard. When working with smaller CubeSats like the 1U CubeSat, helical antennas for sub 2 GHz operation are not feasible since they need to be stowed inside the CubeSat's structure, occupying space needed for other subsystems. With larger CubeSat structures (2U and larger), the available space is larger and thus helical antennas stand as a good solution, having high-gain, wide bandwidth and circular polarization.

In [16], an UHF helical antenna for CubeSats is developed. Due to the low frequency (400 MHz), the helical design would result in a long antenna, thus the engineers made the antenna from a flexible copper adhesive tape, connected to thermoplastic composite strips, folded in a way that the antenna could fit in 0.5U. After release, the springs would be deployed only with their own stored strain energy. The antenna had 13 dBi of gain at 400 MHz and a low axial ratio. Like the ISTsat-1, the GOMX-1 2U CubeSat [6] also had an ADS-B payload. It had a deployable helical antenna, designed to resonate at ADS-B frequency. In the stowed configuration the GOMX-1 ADS-B antenna occupied 0.2U of the 2U CubeSat and on the deployed configuration it extended up to 40 cm, achieving a gain of 10 dBi at 1090 MHz.

2.2.3 Patch Antennas

Patch antennas, also referred as microstrip antennas, are described as antennas that have a conducting patch on one side of a dielectric and a ground plane on the other. These antennas are lightweight, have a low volume and can be built to have a small profile since the thickness is much smaller than a wavelength at resonance frequency. Patch antennas are also relatively low cost, since they can be easily mass fabricated using well known Printed Circuit Board (PCB) etching techniques. Patch antennas can be designed with many different geometries, from a simple square to more intricate fractal shapes.

The simplest method to analyze the patch antenna is with the transmission line model [17]. The transmission line model even though being the least accurate, it provides good physical insight. A rectangular patch antenna can be represented by two radiating slots of width W and height h, separated by a transmission line of length L. Since the dimensions of the patch are not infinite, the EM fields will experience fringing at the patch's edges. Figure 2.4 illustrates the fringing effect on a rectangular patch antenna.

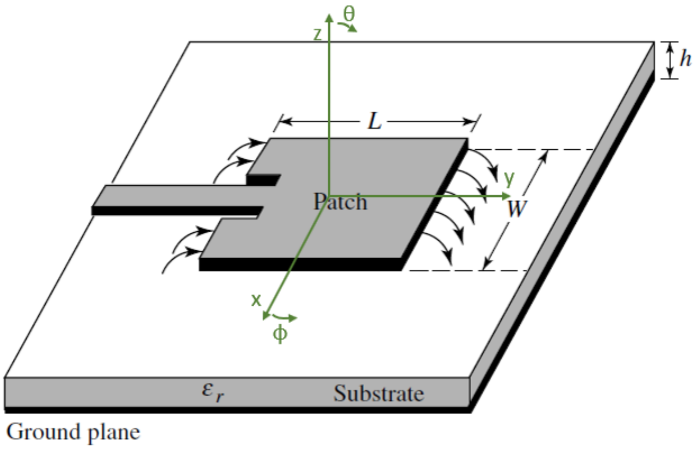

Figure 2.4: Rectangular patch antenna, adapted from [12].

It is the fringing of the fields that are responsible for the radiation by the patch antenna. As seen in figure 2.4, the fringing fields at both edges of the patch are traveling in the same y direction. Considering $L = \lambda/2$, the fields will add up in phase, resulting in a maximum of radiation for $\theta = 0°$ (broadside radiator).

The main design parameters of a rectangular patch antenna are, the length L, the width W, the height h, and the feed point. A patch antenna is normally designed to radiate at its fundamental mode and its resonating frequency f_r is given by

$$f_r = q\frac{c_0}{2L\sqrt{\epsilon_r}}, \tag{2.3}$$

where q is defined as the fringe factor, c_0 the speed of light in vacuum and ϵ_r the dielectric constant of the substrate. The fringe factor q, accounts for the extra electrical length imposed by the fringing fields. The width relates to the bandwidth, as wider patches can achieve larger bandwidths. The height relates to the efficiency and also the bandwidth, as both increase with the increase of the height (if no surface waves are excited). Finally, the feed point relates to the input impedance and it is normally chosen to be 50 Ω in order to interface with the 50 Ω input impedance of the RF electronic front-end. It is important to note that this analysis is good for a first approximation of the antenna design, however, full-wave simulations are always necessary to better understand how the antenna will perform and how can it be optimized.

In satellite applications, the antenna's polarization is an important characteristic. In order to lower the effect of polarization mismatch, circular polarization is usually preferred. Rectangular, square, or circular patch antennas with feeds techniques, like probe feeding or microstrip line feeding, can radiate linearly or circularly polarized EM waves. In patch antennas, circular polarization is achieved if two orthogonal modes are excited with a 90° phase difference. This can be done with many different methods. One can be by feeding the patch in two adjacent sides with out-of-phase signals, provided by a 90° hybrid [18]. Another method is by feeding a square patch in one of the square's diagonals [19] or by truncating two of the patch's opposing corners [20]. Finally, methods like using slots [21] or split ring resonators [22] can also be used.

Patch antennas stand as a good solution for CubeSat applications, especially at high frequencies, where the length of the patch is much smaller than the CubeSats minimum dimension, resulting in a small form factor. There are although some limitations with this type of antennas. Patch antennas usually have low bandwidth, low gain, can cause the excitation of surface waves and although there are many techniques to get circular polarization, polarization purity is hard to achieve. For lower frequencies e.g. L band it is needed a dielectric material with high electric permittivity in order to bring the antenna's physical size down, while maintaining its electrical length. This has the disadvantage of reducing the antenna's bandwidth and efficiency, due to the confinement of the fringing fields and the material's greater losses respectively.

As an example of a patch antenna that would fit in a 1U CubeSat, in [21] a circularly polarized circular patch antenna for the L band (1 GHz) is proposed. The diameter of the circular patch was 66.62 mm and the height of the substrate was 3.2 mm, with $\epsilon_r = 2.6$. The circular polarization and the size reduction where achieved by introducing unequal length slots on the patch. The obtained gain is low, being 7.5 dB lower than an identical antenna without the cross slot. It is then evident, how it is challenging to develop a good performing (miniaturized) antenna, for the small 1U CubeSat. As mentioned before, patch antennas can also be miniaturized using materials with high dielectric constant. In [23], a square patch antenna with tapered peripheral slits is developed to work at 436 MHz. The tapered slits also contribute for the size reduction as well as the high electric permittivity material (RT/duroid® 6006) with a dielectric constant of 6.15. The final dimensions of the antenna were 93 x 93 x 6.4 mm^3 and thus compatible with the CubeSat structure. Due to the extreme miniaturization, the performance of the antenna is highly affected as the antenna only obtained 3.2 MHz of bandwidth and 0.6 dBi of gain.

2.3 Millimeter Wave Antennas

This section presents two types of antennas that are relatively compact and can be designed to work in the millimeter band (30 - 300 GHz), and the slightly lower frequency of the Ka band (26.5 - 40 GHz). In each sub-chapter, the working principles of such antennas are explained as well as some applications within the satellite domain. The study presented in this section is important for this thesis as it shows two different antenna solutions, for the Ka band antenna, presented in chapter 4.

2.3.1 Reflect Array Antennas

When choosing an antenna type that provides high gain and ability of beam-steering, it is usual to think of aperture antennas like the reflector antenna and the lens antenna, or even antenna arrays. Aperture antennas are usually quite bulky and in order to have beam-steering capabilities, the antenna has to be integrated on a mechanical jig that rotates the feed or the whole antenna system. This makes the use of aperture antennas in satellite applications quite costly since the launch cost increases with the payload weight. Antenna arrays or phased arrays, can be a lighter solution that is capable of beam-steering. This is possible by feeding the different array elements, with signals with a prescribed relative phase distribution, in order to vary the direction of maximum radiation. This is usually done with complex feeding networks that can be prone to losses, especially in the millimeter band.

Reflect Array (RA) antennas combine the working principles of reflector antennas and phased array antennas. They can be designed to have high gain and beam-steering capabilities. In RA antennas there is a feed, usually an aperture antenna like a horn antenna or a planar antenna like a patch, and a planar surface where the unit cells are located. Figure 2.5 illustrates how an RA antenna is usually configured, with the feed represented as an horn antenna, radiating towards the RA surface, which consists of periodic square patches.

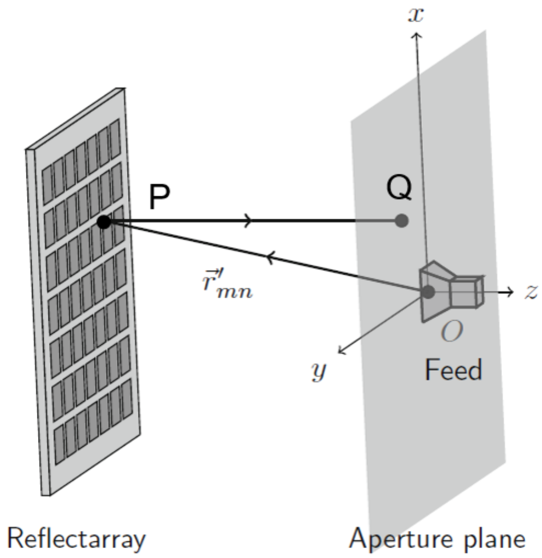

Figure 2.5: Reflect array antenna configuration, adapted from [24].

The working principle of the RA antennas can be explained by considering each individual unit cell as an EM scatterer. To mimic the effect of the curved reflector of a reflector antenna, the unit cells must impose a phase shift on the incident wave so that it compensates the electrical path length differences. This path length relation is given by

$$-k_0(\overline{OP} + \overline{PQ}) = constant, \tag{2.4}$$

for every point P in the array surface, being k_0 the free space wavenumber. Considering the case where the aperture plane is parallel to the RA's surface, the distance $\overline{PQ}$ is not needed in equation 2.4 because it is equal for every unit cell. Each unit cell introduces a phase shift ψ_{mn}, between the incident and the reflected wave. Considering also that the unit cells are laid out in an m x n matrix, the RA design equation is given by

$$-k_0 r'_{mn} + \psi_{mn} = constant, \tag{2.5}$$

being mn the position of the unit cell on the matrix and r'_{mn} the distance between the feed and the unit cell. The phase shift ψ_{mn}, introduced by each unit cell, is of utmost importance when designing an RA antenna, because a small shift from the desired value could alter greatly the performance of the antenna. The next section presents different types of unit cells that can be designed, in order to obtain the wanted phase shift.

Unit Cell Design

The unit cell designs can be divided into two categories, the phase delay, and the phase rotation unit cells. In the phase delay unit cells, the phase shift is obtained by changing one or more dimensions of each cell's geometry, comparing to a reference cell. By doing this, the equivalent refractive index is changed locally, and thus delaying the phase, just like in a transmission line. The unit cell geometry can be, for example, a simple square patch. Where by varying the patch length, a phase shift can be obtained, due to the shift in resonance. Ideally, the phase range for resonance frequency is wanted to be the 0° to 360°. Even though the phase distribution at the RA surface can have values over 360°, the phase shift is always relative to one unit cell, and it can be wrapped to be in the 0° to 360° range. In reality, for simple unit cell geometries like the square patch, the whole 0° to 360° is usually not achieved. This is due to limited unit cell size, and it comes from the fact that it is needed a lot cells to introduce a different effective permittivity, and without blocking the incoming wave, thus the need of being small in relation to the wavelength. There are many phase delay unit cells designs that can achieve the full phase shift range, one of those being the dual-resonance unit cell [25], where two elements introduce two different resonances, increasing the obtained phase shift.

In the phase rotation unit cells design, instead of altering the unit cell's dimension, it is the physical angle of rotation of the unit cell that introduces the phase shift, comparing to a reference cell. One example of this, is rotating a ring resonator on its own z axis and thus creating a phase shift [26, 27]. Figure 2.6 illustrates how a simple circular split ring resonator can be rotated by an angle α. In sequential rotation unit cells, a physical rotation of α corresponds to a phase shift of 2α. One advantage of this unit cell design is that, for circular polarization a lower axial ratio, and higher axial ratio bandwidth, can be achieved.

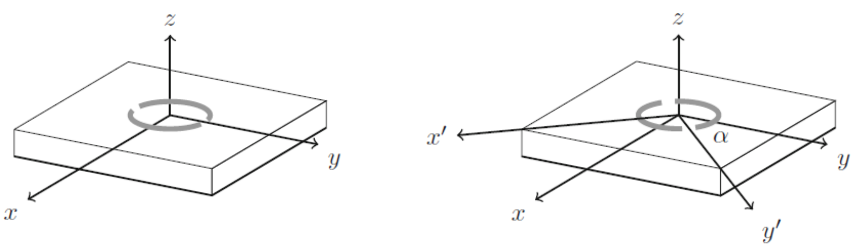

(a) Unrotated cell. **(b)** Rotated cell.

Figure 2.6: Unrotated and rotated circular split ring resonators [24].

When designing and simulating the unit cells, there is an important approximation done in order to obtain the phase shift variation. When simulated in an numerical EM solver, the single unit cell is considered to be in an infinite periodic structure, with identical cells all around. The phase shift variation is calculated considering the whole structure, as the phase variation couldn't be studied with a single unit cell, due to its size being much smaller than one wavelength. This a good approximation for designing the unit cells where the change in geometry between adjacent cells is small. In areas where this change is large, the approximation is not so accurate, but because these areas account for a small percentage of the overall RA surface area, the resulting error in the radiation pattern is small.

2.3.2 Transmit Array Antennas

Like the RA antennas discussed in the previous sections, Transmit Array (TA) antennas are also of the planar type with high-gain and having beam-steering and beam-shaping capabilities, while having a compact form factor. On the contrary to RA antennas,TA antennas work in a transmission mode, where the incident wave is modified when it propagates through the TA structure, just like a lens. TA antennas offer some advantages over RA antennas, such as easiness of integration, since the feed is behind the array surface and thus it is not susceptible to blocking effects by the feed, like in the RA. On the other hand, the design and optimization of TA antennas is more complex than RA antennas.

A generic model of the TA can be considered, where the unit cell is composed of a receiving part, a transmitting part and a phase-shifter interfacing both. Figure 2.7 illustrates this generic model.

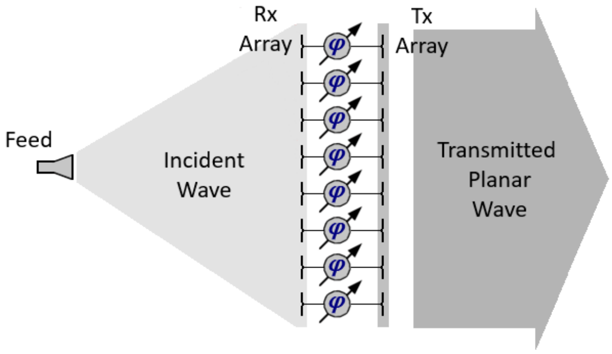

Figure 2.7: Transmit array antenna configuration, adapted from [28].

The phase-shifting at unit cell level can be implemented using different techniques, resulting in different unit cell designs. Also, the unit cells can be constituted of multiple layers. The next section gives an overview of some possible designs for these unit cells.

Unit Cell Design

It is of utmost importance the good design of the unit cells of an TA antenna, because not only the cells need to provide the needed phase shift, the transmission between the receiving face and the transmitting face needs to be as high as possible, by minimizing the reflection coefficient at the input side of the cell. The latter makes the design of TA antennas more complex, comparing with RA antennas. Just like in the RA antennas, the unit cells design can be divided in two main categories, phase delay, and phase rotation unit cells.

For the phase delay unit cells, different phase shifts can be obtained by changing some design parameters, like varying the unit cells dimensions. The phase shift variation with only one layer is far from the wanted 2π of excursion, so multilayers have to be used. It is needed at least 4 layers of a Frequency-Selective Surface (FSS) to get a 2π phase shift range [29]. Meaning that for $S_{21} \geq -1$ dB the whole 2π phase shift excursion can be achieved. With the phase rotation unit cells only one layer is needed to achieve the full range of phase shift, resulting in lighter and less thick solutions, for circularly polarized waves.

2.3.3 Beam-Steering

RA and TA antennas can be developed to allow for beam-steering capabilities. In recent years, there has been a lot of research in this area since there are a lot of applications that can benefit from these antenna functionalities. Applications like inter-satellite communications, wireless broadband, synthetic aperture radar, point-to-point terrestrial links and deep-space communications.

There are three main ways of developing beam steerable RA and TA antennas. This can be achieved using mechanical beam-steering, switched-beam techniques and reconfigurable RA and TA.

In the mechanical beam-steering, for the RA antenna, the feed or the surface can be rotated to steer the beam. For the TA antenna, the TA surface can be rotated around its center, translated or have in-plane rotation in order to change the direction of maximum radiation. In [30] a circular polarized TA antenna for the Ka band satellite communications, with wide beam-steering by in-plane translation is proposed. By mechanical translation of the TA surface, the antenna achieved 0° to 50° elevation scan and full azimuth coverage by rotating the TA by 360° on the surface plane.

In the switched-beam technique there are more than one feed antennas, designed that each feed has a different focal point in the RA or TA surface, resulting in different directions of radiation at the output. It is called switched-beam because the multiple feeds are multiplexed and switched to get the desired focal point. In [31] a TA antenna working in the V-band for the next generation of mobile networks (5G) is presented. The feed of the TA consists of an array of five patches that are multiplexed. With that array as a feed, the antenna was able to produce five diferent beams at the output and a 3 dB angular coverage of 13.2°.

In regards to the reconfigurable RA and TA antennas, the switching and tuning capabilities are integrated in the unit cell. Table 2.2 describes the enabling technologies for reconfigurable RA and TA antennas.

Table 2.2: Applicable technologies for reconfigurable reflect array antennas, adapted from [32].

Type	Technology	Maturity	Control	Complexity	Loss (microwave)	Bias Power Consumption	Linearity	Switching Time
Lumped Elements	PIN diodes	High	Digital	High	Low	Low	Mod.	High
	Varactor diodes	High	Analog	High	Low	High	Low	High
	RF-MEMS	Mod.	Digital	High	High	High	High	Mod.
Hybrid	Ferroelectric thin film	Mod.	Analog	Mod.	Mod.	High	Mod.	High
Tunable Materials	Liquid crystal	Mod.	Analog	Mod.	Low	Mod.	Mod.	Low
	Graphene	Low	Analog	Mod.	Low	High	Low	High
	Photoconductive	Mod.	Analog	Mod.	Low	Low	Low	High
Mechanical	Fuidic	Mod.	Analog	Mod.	Mod.	High	Mod.	Low
	Micromotors	Low	Analog	Low	High	Mod.	High	Low

2.3.4 Space Applications

RA and TA antennas stand as a good solution for space applications that require a high-gain, compact size antennas, that can be designed to provide beam-steering and beam-shaping capabilities. Comparing with the bulky reflector antennas and the phased array antennas, where in the millimeter wave band can be very lossy and of complex design.

One possible application for the use of RA antennas is Earth observation, for example using synthetic aperture radar technology [33] and cloud and precipitation monitoring [34]. In synthetic aperture radar applications, the use of high-gain antennas is desirable so that the overall imaging system has good sensitivity and resolution for the imaging of specific areas on the Earth's surface. Also, to mitigate the attenuation in the atmosphere, that with increasing operational frequency starts to impact the overall system performance.

Another application for RA antennas is inter-satellite communication [35, 36]. With the increase in the amount of data that the satellites have to relay between themselves and ground stations, high-gain antennas at high frequencies of operation (millimeter band) are desirable because they allow for higher data throughput. Beam-steering and beam-forming capabilities are desired as well, in applications where the satellite needs to keep pointing to other satellites e.g., in a satellite constellation.

When designing these types of antennas to be implemented in CubeSats, one should also consider how they will be stored and deployed within the CubeSat structure. Even though RA antennas are more compact than reflector antennas, they are still usually bigger than the CubeSat structure in order to have a large antenna aperture. In [34] the dual-band RA antenna for the Ku/Ka bands has a length of 0.5 m and in [33] the main Ka band RA antenna as a length of 1.8 m, resulting in a high gain of 50 dBi. With this in mind, deployable RA antennas are needed in order to integrate them in the CubeSat's small structure. NASA's engineers in the ISARA CubeSat [37], took advantage of the deployable solar panels of the 3U CubeSat and implemented an RA antenna on the backside of the panels. Figure 2.8 illustrates ISARA's antenna configuration in both stowed and deployed states, on the 3U CubeSat structure. The antenna, when the system was fully deployed, achieved a gain of 33.5 dBi at 26 GHz. Another approach

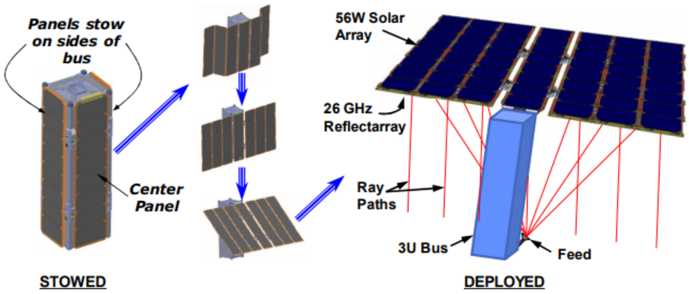

Figure 2.8: ISARA's reflect array antenna in stowed and deployed states [37].

that can be used for integrating the RA antenna in the CubeSat, is by designing the RA to work on top of the solar panels [38], designing unit cells that only have very little impact on the performance of the solar panels.

Just like the RA antennas, TA antennas also stand as a good solution for space applications, due to their high-gain, beam-steering capabilities while maintaining a compact size, comparing to the larger reflector antennas. Due to their discussed capabilities, TA antennas are a good solution for high data rate links, like in broadband satellite communication systems [39, 40]. Moreover, in satellite communications the up-link and the down-link are realized in two different frequency bands and with orthogonal polarizations. This results in the need of using two different antennas, which occupy double the space needed, comparing with a one antenna solution. Although very complex, this is possible in TA antennas and solutions for the design of unit cells that allow for dual-band operation has been recently researched [41].

TA antennas can also be integrated in smaller satellites like the CubeSat but in a deployable form, if the antenna aperture is large. Another detail to have in consideration is the maximum focal distance available within the CubeSat structure. There has been some research on ways to decrease the focal distance between the feed and the TA surface, methods like using multiple feeds [42], creating virtual focus points using intermediary arrays [30], using leaky waveguides [43] and metasurfaces [44].

2.4 Space Related Antenna Issues

As mentioned previously, when designing antennas for space applications, there are much more issues to take into consideration comparing with antennas designed to work on the Earth. In this section, a detailed explanation of some hardships and challenges that are usually experienced when designing and launching antennas to space, for small satellites, is presented.

2.4.1 Temperature Variation

The temperature variations that satellites and antennas experience in space is much greater than the one experienced in normal conditions, on Earth. Antennas for space applications should be made of materials that behave well under large and continuous temperature variations. Materials expand and contract with temperature changes, this can be detrimental to the antenna's performance, as the physical size of the antenna is sometimes related to it's resonance frequency. Considering this, the selected materials should have a low thermal expansion coefficient, and preferably identical in every axis, so that the deformation is uniform. Also, as the antennas are mounted onto the satellite structure, their thermal expansion coefficient should be similar to the structure's, to minimize mechanical stress. For antennas that have dielectric materials, the thermal coefficient of the dielectric constant is also important. Ideally, it is wanted materials with a low thermal coefficient of dielectric constant, so that the material permittivity varies less with temperature changes, resulting in smaller frequency shifts.

2.4.2 Outgassing

Being space a high vacuum environment, some materials can experience outgassing. Outgassing consists of the release of gasses that are trapped within solid materials. These gasses can contaminate other subsystems on the satellites, such as image sensors, lenses, mirrors, and solar cells. With this in mind, when developing planar antennas for space, materials with low outgassing properties must be chosen. Specifically, materials with a total mass loss higher than 1.0%, and collected volatile condensable materials over 0.1% [45], should be avoided in space applications.

2.4.3 Atomic Oxygen

Atomic Oxygen can be found in low earth orbit, between 100 and 1000 km. This atomic version of oxygen is created by the interaction of UV light and molecular oxygen. These atoms are very corrosive and, over time, will oxidate metals, specially silver and osmium, and will erode polymers [46].

2.4.4 Electrostatic Discharge

When an orbiting satellite passes through an area of high plasma activity or gets bombarded with charged particles, its surface and the exposed subsystems surfaces' will build-up with surface charges. These charges will create a high voltage potential between these surfaces and other components/surfaces. This can be the cause of many problems, such as dielectric breakdown, arcing, produce single-upset events, and damage electronic systems [45]. Materials like RF sunshields can be deposited on planar antennas, in order to mitigate this problem [47].

3

ISTsat-1 Antenna

Contents

ISTsat-1 Antenna

In this chapter, the development process of the ISTsat-1 antenna is presented. First, the ISTsat-1 mission and its requirements, regarding the ADS-B antenna is analyzed. Then, the design of the antenna solution, is presented. Finally, the development of two prototypes is also presented, one pre-prototype and the final antenna prototype.

3.1 Problem Overview

In the ISTsat-1 ADS-B mission, the satellite receives ADS-B signals from airplanes, calculates multiple statistics from this data, and sends it to ground stations using UHF and VHF bands. The ADS-B antenna system mounted on the airplanes usually consists of two quarter-wave blade antennas, one mounted on top of the fuselage and another on the bottom. These antennas have linear polarization, and their generic radiation pattern is illustrated on figure 3.1(a). When mounted onto the airplane fuselage, the blade antenna's radiation pattern is affected and stops being axial symmetric. This radiation pattern is illustrated in figure 3.1(b). For the top-mounted antenna, its radiation pattern presents a null at the airplane's zenith, causing an area of zero coverage with increasing diameter, at higher altitudes.

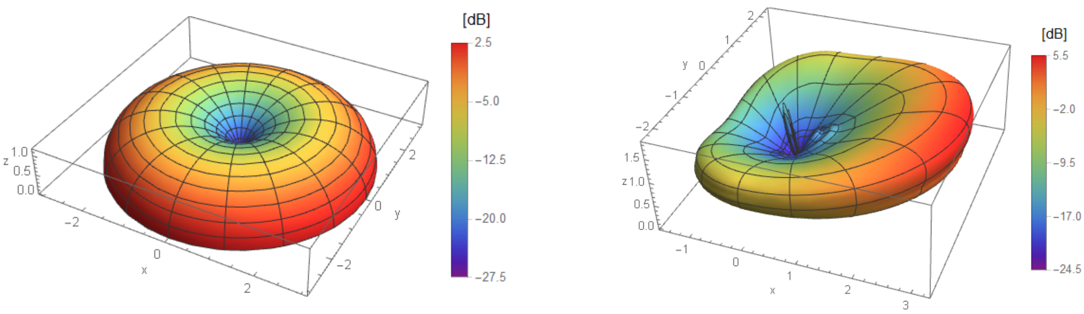

(a) **(b)**

Figure 3.1: Monopole radiation pattern. (a) Ideal, over an infinite ground plane. (b) Mounted on an airplane, adapted from data in [48].

ISTsat-1 will orbit at 400 km of altitude, with the bottom face normal to the Earth's surface, and an expected tumbling rotational speed of 5 degrees/s, in the normal axis. Considering that the UHF and VHF antennas are located in the top of the satellite and the sides covered with solar panels, the only space left to mount the ADS-B antenna for this mission scenario is in the satellite's bottom face. Figure 3.2 illustrates the ADS-B link scenario, where the satellite's ADS-B antenna is mounted on the bottom face and is communicating with a monopole antenna located on the top of the airplane's fuselage.

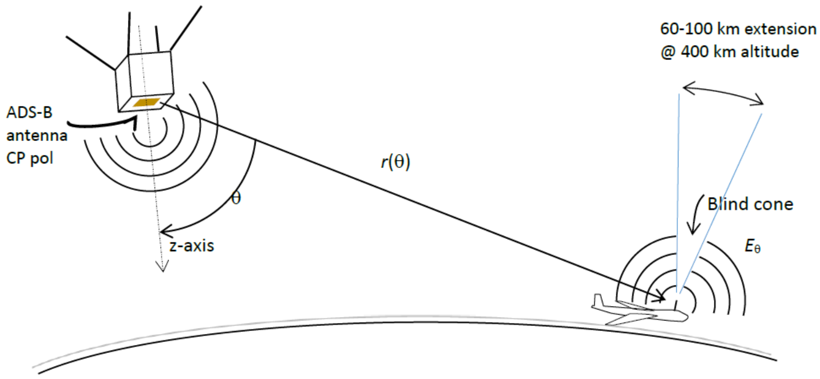

Figure 3.2: ADS-B link scenario.

As mentioned in 2.2.3, the polarization of antennas is an important characteristic, as some polarization configurations can cause higher polarization mismatch, for example with two antennas with orthogonal linear polarizations, where the attenuation due to polarization mismatch is maximum, and thus degrading the communication links. Regarding this mission, circular polarization is found to be the best polarization for the ADS-B antenna. In spite of losing 3 dB in the communication link, due to the mismatch between the linear polarized blade antenna on the airplane and the circular polarized antenna on the ISTsat-1, the circular polarization makes the satellite's ADS-B antenna insensitive to the position and direction of which the plane is travelling, in regard to polarization.

In this CubeSat mission there are more requirements and challenges that influence the choice of the ADS-B antenna that will be integrated onto ISTsat-1's bottom face. It is important to note that, with all the other subsystems inside the CubeSat, the available space to mount the ADS-B antenna, is only 100 x 100 x 5 mm^3. Even if it is possible to fit a deployable solution in the small volume, this is solution is undesirable for this mission. Deployable solutions would increase the probability of failure and are very challenging to make mechanically robust, which is needed due to the high g-forces and vibrations that the CubeSat will experience upon launch. Additionally, a deployable solution would require extensive reliability tests, which are not compatible with the budget or timeline of this thesis. There are other issues, like the large temperature variations experienced in space, and material outgassing, and the need for more volume inside the CubeSat. These are explained with more detail in section 2.4.

3.1.1 Link Budget

The link budget is an important study to be made when working with a wireless communication link. Regarding the ISTsat-1's ADS-B antenna, it is needed to calculate the necessary antenna gain, in order to receive the ADS-B signals. The Friis transmission equation can be used to calculate the power of the signal at the receiving antenna. The power at the receiver is given by,

$$P_r = \frac{P_t G_{sat}(\theta_s, \phi_s) G_{acraft}(\theta_c, \phi_c) \lambda^2}{(4\pi r)^2} c_p c_z L \tag{3.1}$$

being P_t the aircraft's transmit power, G_{sat} the satellite's ADS-B antenna gain, G_{acraft} the aircraft's ADS-B antenna gain, λ the ADS-B carrier frequency, r the line of sight distance between satellite and aircraft, c_p the polarization mismatch loss, c_z the impedance mismatch loss, and L representing the propagation losses.

Equation 3.1 was rewritten to express G_{sat} in terms of the other variables, in order to calculate the necessary minimal antenna gain for the satellite ADS-B antenna so that the satellite's ADS-B receiver could decode the messages. The considered transmitted power was 500 W, which is the maximum power transmitted by commercial airplanes, and the receiving power was -95 dBm, which is the lowest signal amplitude that the ISTsat-1's ADS-B receiver can receive, also known as sensitivity. Then, for the aircraft's antenna gain, two cases were considered. One, for an ideal monopole and another for the more realistic case, whose radiation patterns are represented on figure 3.1(a) and 3.1(b), respectively. The polarization mismatch was chosen as -3 dB to account for the circular/linear polarization mismatch, and the atmospheric losses were not accounted for. Figure 3.3 illustrates the necessary gain for the ADS-B antenna on an 800 x 800 km^2 area, where each pixel represents the necessary antenna gain for one position of the airplane, for the link budget to be fulfilled.

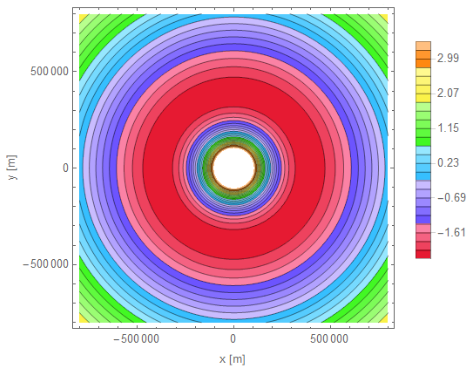

(a)

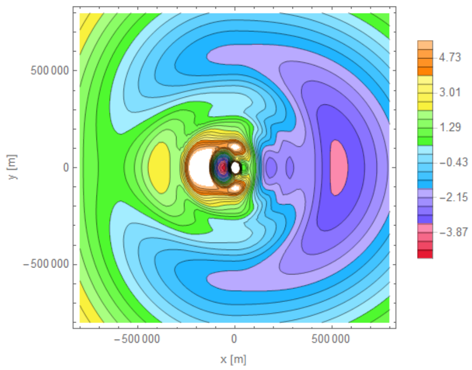

(b)

Figure 3.3: Footprint of necessary satellite antenna gain, in dB. (a) Airplane with ideal monopole antenna radiation pattern. (b) Airplane with realistic antenna radiation pattern.

It can be observed, both in figure 3.3(a) and 3.3(b), that with an antenna gain of 0 dB, a good coverage of the defined area can be obtained. With this in mind, the proposed antenna solution for the ISTsat-1's ADS-B antenna has to have 0 dB or higher gain. In reality, an antenna gain around 1 - 4 dB would be optimal, to account for possible losses on the communication link.

3.2 Antenna Design

Considering all the requirements presented above, and the antenna solutions, presented in chapter 2, the circularly polarized patch antenna is chosen as the best solution. When designing a circularly polarized patch antenna, many different characteristics must be considered in order to achieve the desired performance. These characteristics include substrate permittivity and height, patch geometry, and feeding technique.

Regarding the substrate electric permittivity, a substrate with a high permittivity ($\epsilon_r > 4$) must be chosen due to the large wavelength at 1090 MHz ($\lambda = 27.5$ cm), comparing with the available space in the 100 x 100 x 5 mm^3 CubeSat bottom face. A substrate with a higher value of permittivity allows for a reduction in the physical size of the antenna, while maintaining its electrical length. This comes at a cost, as higher permittivity substrates usually have higher losses, decreasing the antenna's overall efficiency. Also, the obtained bandwidth is lower compared to lower permittivity substrates, as the fields are more confined in the high permittivity substrate, resulting in poorer radiation by the antenna. For this specific application, a small bandwidth is preferred due to the reduction of temperature noise at the receiver input.

Another antenna parameter that affects the bandwidth is the substrate height, as higher substrates allow for higher bandwidths. The height of the substrate is also related to the antenna's efficiency and generally, for electrically small antennas, the efficiency increases with higher substrate heights. The trade-off with choosing higher substrates is that as the height increases there is a possibility of exciting surface waves and thus degrading the overall antenna radiation pattern.

As stated in 2.2.3, there are many techniques and patch geometries to achieve circular polarization. For this antenna it was chosen the square patch with truncated corners, as it is a stable, well known solution, that is well characterized in the literature. Figure 3.4 illustrates such geometry.

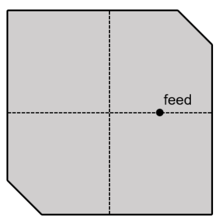

Figure 3.4: Geometry of square patch with truncated corners.

As previously explained in 2.2.3, the length of the square patch is chosen so that it resonates at the desired frequency, and the truncated corners introduce two degenerate orthogonal modes, ideally 90 degrees out of phase, in order to achieve circular polarization.

Regarding the feeding technique, this antenna needed a low profile, easy to assemble feed, due to the small available space inside the CubeSat. The probe feed presented itself as the best option. Comparing with the microstrip line feed, the probe feed does not need a microstrip line at the patch's surface and also allows to have the connector closer to the center of the patch, away from the ISTsat-1's structural pillars. Another option is the slot feed, but it introduces the added complexity of layer superposition. Due to the antenna height restriction, a low profile connector is used, of the MMCX type.

Lastly, it is important to note that the substrate material used in this application must be space rated and have low outgassing characteristics. The material should also have a low dependency of temperature, regarding its electric and physical properties.

3.3 Antenna Pre-Prototype

The first antenna prototype was designed to be fabricated in FR-4 substrate. FR-4 is a relatively cheap substrate material that is widely used in electronic PCB fabrication. FR-4 is also widely used for commercial antennas, for example for cellphones and IoT devices. Being quite lossy, this material is not very used for antenna applications where the specifications are tight, e.g. space applications. Despite this, designing and fabricating a prototype in FR-4 was a good preliminary stage option, in order to characterize the accuracy of our fabrication and measurement set-ups, before using more expensive substrate materials.

3.3.1 Material Permittivity Measurement

Due to high uncertainty on the FR-4 permittivity value, it was necessary to measure the permittivity of the material. This uncertainty of the permittivity value of the materials, affects the resonant center frequency of the antenna, and in the applications where the bandwidth is small, like for this antenna, the resonant shifts can result in a fabricated antenna not resonating at the desired frequency. The uncertainty on the permittivity value of the more expensive, space rated substrates, still exists but it is usually very small. The measurement is based on [49], where an indirect method for calculating the complex permittivity of polylactic acid, using a transmission line circuit with resonant stubs, is presented.

The microstrip circuit, fabricated in FR-4, used on this thesis, consists of a radial stub designed to have a notch at 1090 MHz, and four Split Ring Resonators (SRRs) in order to introduce a notch with a smaller bandwidth, to achieve a higher sensitivity and thus measure smaller changes of permittivity.

Figure 3.5 illustrates the circuit used for the permittivity measurements, its dimensions are specified in table 3.1, and the fabricated circuit on figure 3.6.

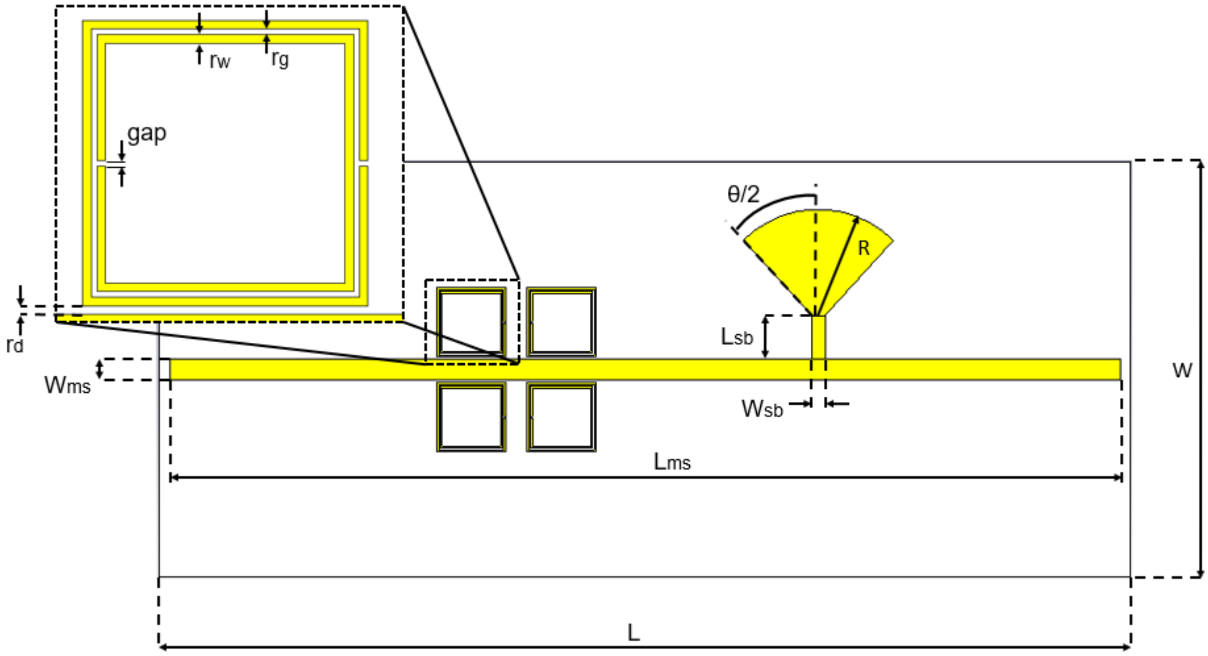

Figure 3.5: Microstrip circuit geometry.

Table 3.1: Parameters dimensions in millimeters.

L	W	L_{ms}	W_{ms}	L_{sb}	W_{sb}
140	60	137	3.1	6.3	2
R	θ	gap	r_w	r_g	r_d
15.3	90°	0.2	0.3	0.2	0.3

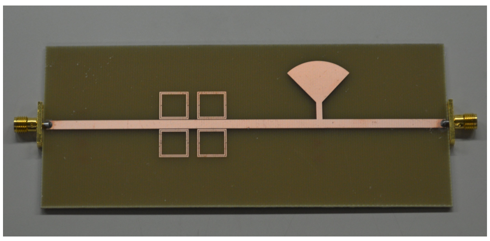

Figure 3.6: Fabricated circuit.

This permittivity measurement method is based on the comparison between measured and simulated reflection and transmission coefficients, as the complex permittivity is related to the amplitude and phase of these coefficients. First, the circuit is simulated, using CST-MWS, and then fabricated. Then the S-parameters are measured and compared to the simulation results. If the results do not align properly, one has to adjust the permittivity in the simulation. The results can also be misaligned due to an error in the simulation, fabrication errors, or poorly modeled connectors. With this in mind, specific procedures are made to guarantee that the frequency shift is only a consequence of the circuit's permittivity. These procedures are, making sure the circuit and its elements are properly matched in the simulation model; doing a superposition of the mask on a microscopic image of the small element details, to see if there was overetching; making sure the 3D model of the connector is identical to the connector itself, and that is properly meshed.

This permittivity measurement method involves iterative simulations until the best alignment of results is found. After the permittivity of the substrate has been calibrated, a superstrate of the material whose permittivity we want to measure is placed on top of the circuit, and the S-parameters are measured once more. Once again, iterative simulations are needed until a good match of the results is found. Figure 3.7 shows the comparison between measured and simulated S-parameter results of the measuring circuit without the superstrate.

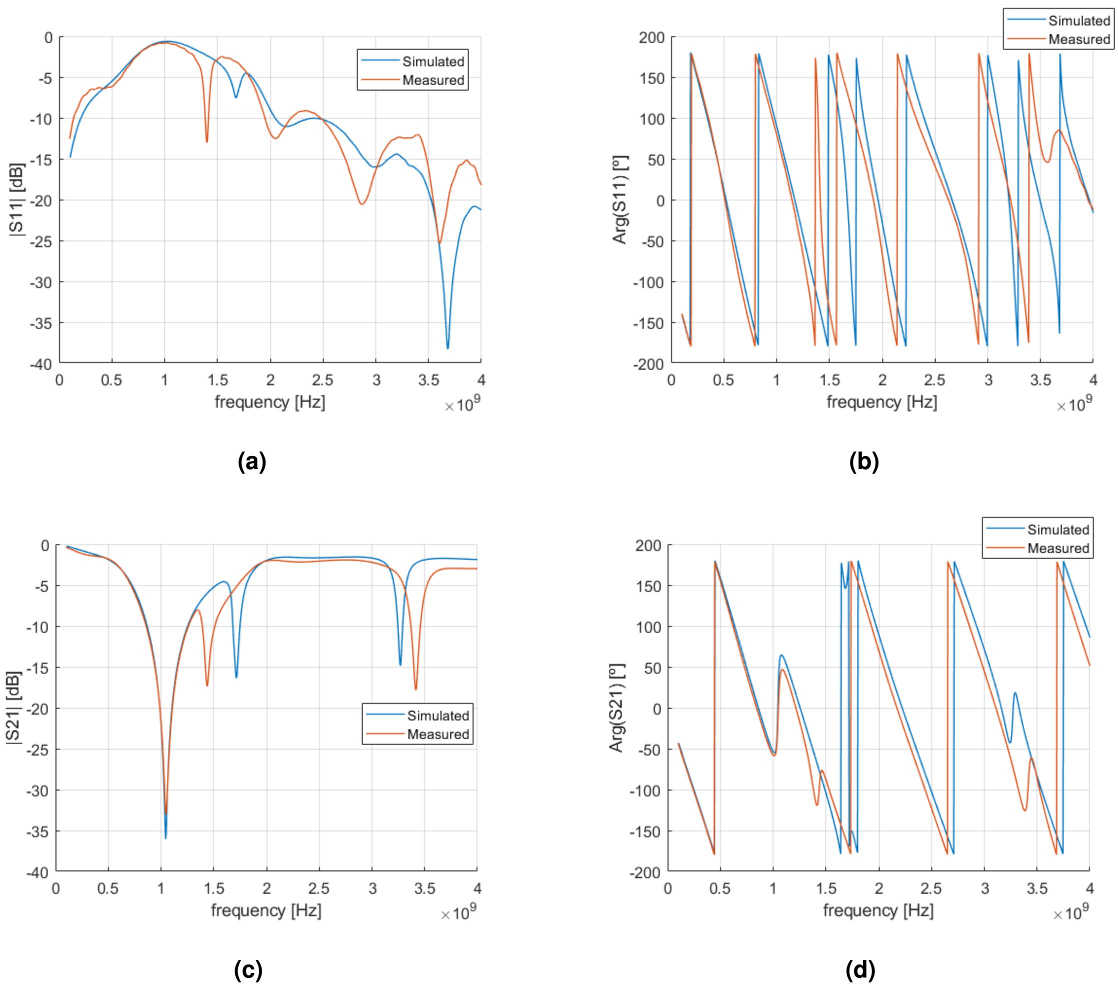

(a) (b) (c) (d)

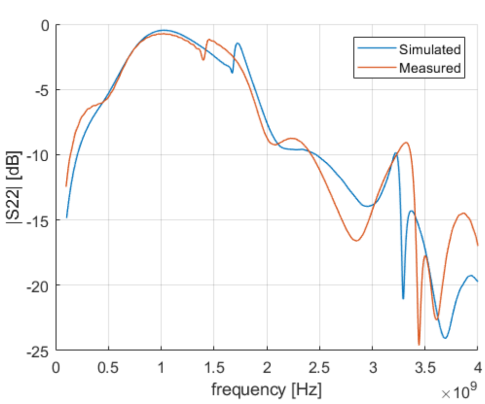

(e)

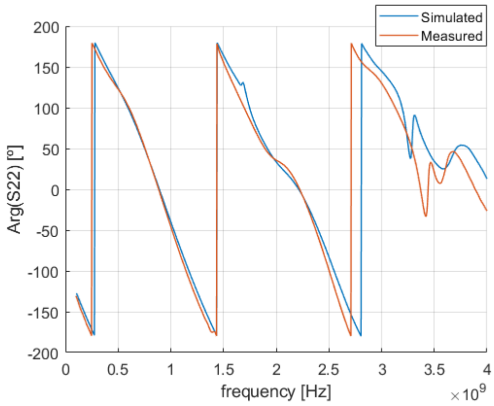

(f)

Figure 3.7: Simulated and measured S matrix results of microstrip circuit. The simulated S-parameters are for a substrate with $\epsilon = 4.65$. (a) S11 Magnitude. (b) S11 Phase. (c) S21 Magnitude. (d) S21 Phase. (e) S22 Magnitude. (f) S22 Phase.

The best results were obtained when the permittivity of the substrate was selected as 4.65 in the simulation. In figure 3.7(c), it can be seen that the stub resonance (1090 MHz) matches nicely between simulated and measured results, but the resonances introduced by the SRRs have a 200 to 250 MHz shift in resonance. The lower resonance was shifted down and the higher was shifted up in frequency. This shift can occur for many reasons, as this is a circuit that is sensitive to fabrication imprecisions. Multiple tests were executed in order to find the source of this error. Tests including, the refinement of the mesh in and around the SRRs, and a fabrication test, where the mask of the circuit was superimposed onto a microscopic picture of the fabricated circuit. Even though the SRRs did not perform as expected, the agreement between the simulated and measured results is good from 0 to 1250 MHz, which includes the frequency of interest (1090 MHz).

After calibrating the circuit, by fixing its permittivity in the simulation as 4.65, new measurements and simulations were done where a FR-4 superstrate was placed on top of the measurement circuit. These S-parameter results are shown in figure 3.8.

A good agreement between measured and simulated results was found when $\epsilon = 4.4$, both in magnitude and phase for the 0 to 1250 MHz band. With these results, it is concluded that the permittivity of the FR-4 substrate used is approximately 4.4. As expected, the permittivity value differs from the one stated in the manufacturer datasheet of 4.8, specified at 1000 MHz.

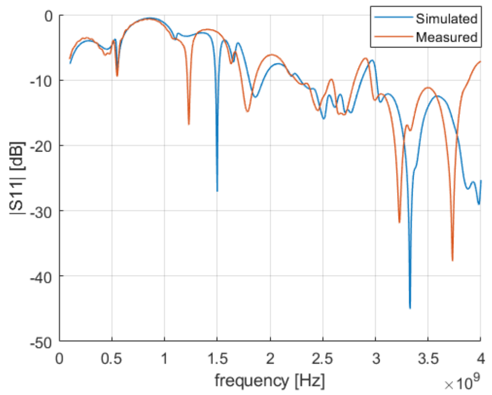

(a)

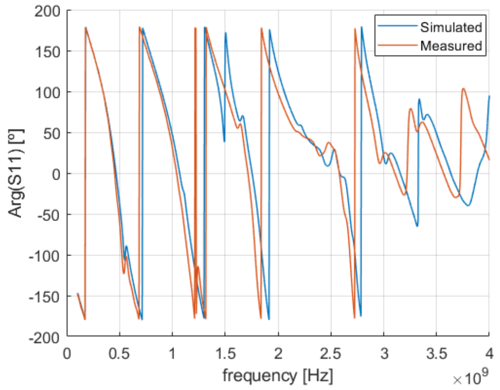

(b)

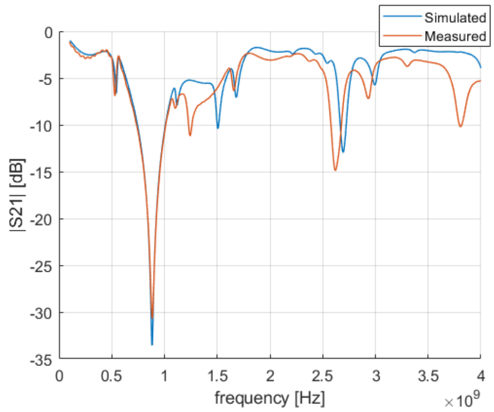

(c)

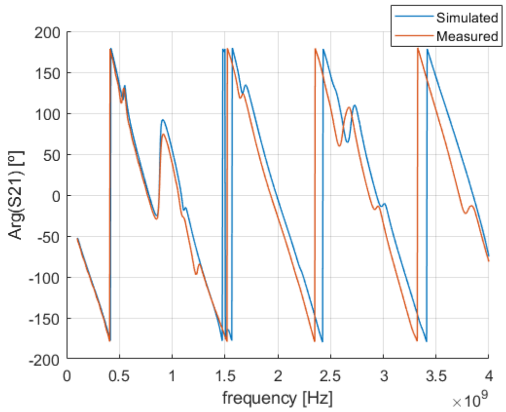

(d)

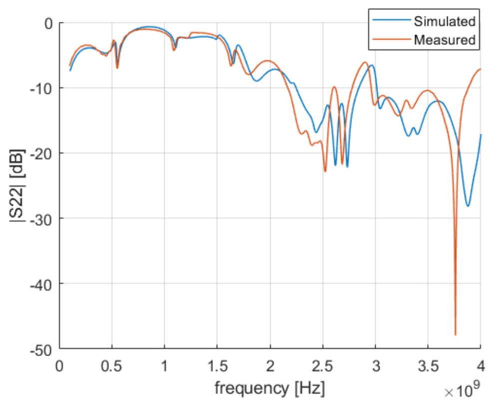

(e)

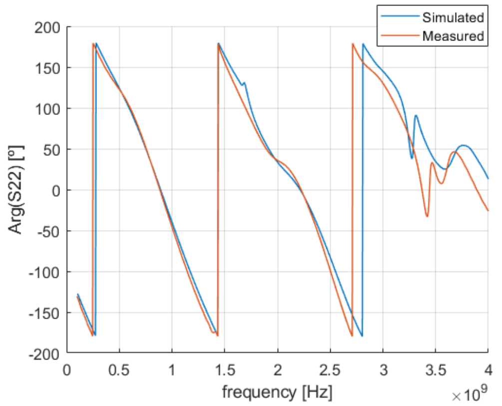

(f)

Figure 3.8: Simulated and measured S matrix results of microstrip circuit with FR-4 superstrate. The simulated S-parameters are for a superstrate with $\epsilon = 4.4$. (a) S11 Magnitude. (b) S11 Phase. (c) S21 Magnitude. (d) S21 Phase. (e) S22 Magnitude. (f) S22 Phase.

3.3.2 Simulations and Measurements

The antenna was designed using CST-MWS, for a substrate with 4.4 of electric permittivity, corresponding to the permittivity measured in the previous step. A first approximation of the patch size was obtained using equation 2.3. Then, the optimization was performed with successive full-wave simulations, where the patch size and the truncated corners were adjusted until the best results were found. The final geometry is illustrated in figure 3.9 and its dimensions are specified in table 3.2.

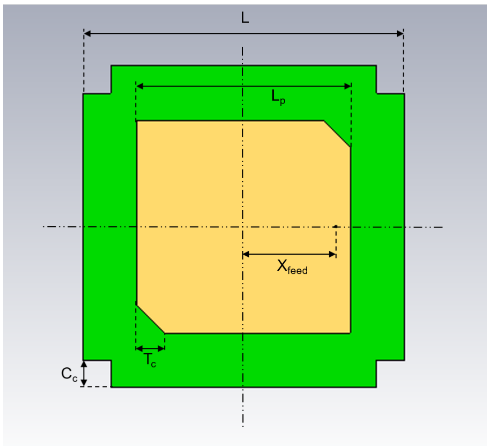

Figure 3.9: FR-4 patch antenna geometry.

Table 3.2: FR-4 patch antenna dimensions in millimeters.

L	L_p	X_{feed}	T_c	C_c
98	64.8	28	8.2	8.5

The designed antenna was then fabricated, using the same FR-4, with previously measured permittivity. The MMCX connector used, is a right angle PCB jack from Amphenol®RF [50]. Figure 3.10 shows the fabricated square patch antenna with the FR-4 substrate.

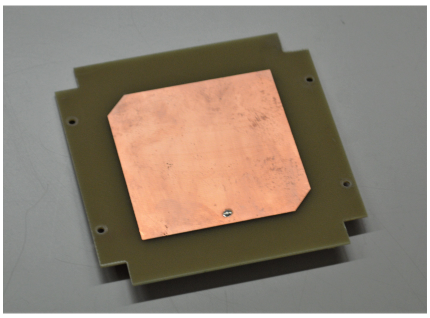

Figure 3.10: Fabricated antenna with FR-4 substrate.

The fabricated antenna's reflection coefficient was measured using a VNA and the measured results were compared to the simulated ones. These results are represented in figure 3.11.

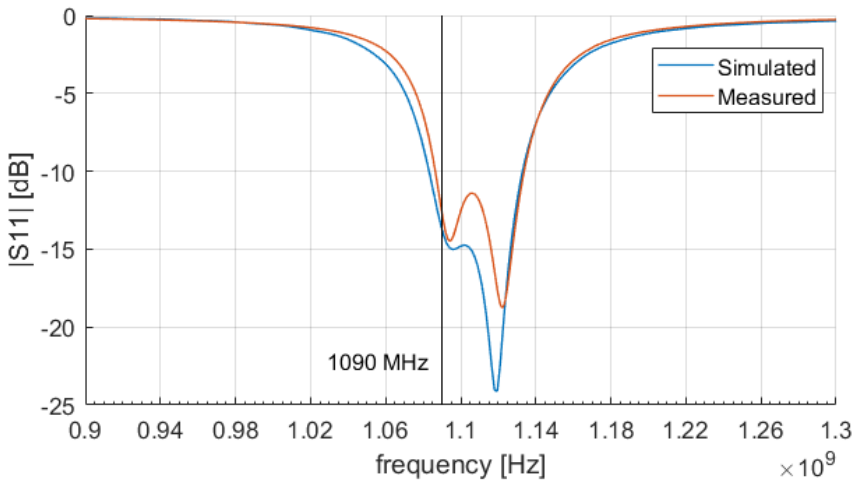

Figure 3.11: Comparison between simulated and measured reflection coefficients.

There is a good agreement between measured and simulated results, in terms of the reflection coefficient. The measured -10 dB bandwidth is 47 MHz, centered around 1106 MHz. The center resonance is shifted from the desired 1090 MHz due to an error of improper meshing in the simulation. Even though the mesh was good, according to the CST-MWS guidelines, it was not refined enough for the small tolerances of this antenna. However, the ADS-B frequency is still inside the antenna's bandwidth, indicating that the fabricated antenna is more than suitable for the preliminary tests. This forms a basis before changing to the final prototype on the more expensive substrate.

The fabricated antenna's radiation pattern was measured in an anechoic chamber and the measured results were compared to the simulated ones. Figure 3.12 illustrates both measured and simulated radiation patterns, in terms of circular right/left (cross/co) polarization, for two planes.

There is an overall good agreement between the measured and simulated radiation patterns, especially for $\theta \in$ [-90°, 90°], for both planes. The cross-polarization level at $\theta = 0°$ is approximately -10 dB, and remains lower than -8 dB, between $\theta \in$ [-50°, 50°]. The measured right polarization field component for the plane $\phi = 90°$ was shifted up 4 dB, possibly due to unwanted reflections on the anechoic chamber walls, as the EM absorber material is only rated to work with frequencies between [1.8, 18] GHz.

The axial ratio, which represents the antenna's circular polarization purity, was also measured in the anechoic chamber. The measured and simulated axial ratio results are represented in figure 3.13.

The obtained axial ratio for the fabricated prototype is always higher than 3 dB, which means that the fabricated antenna is not circularly, but elliptically polarized. The axial ratio is minimum at 4.68 dB, for 1097 MHz, and 5.6 dB for 1090 MHz.

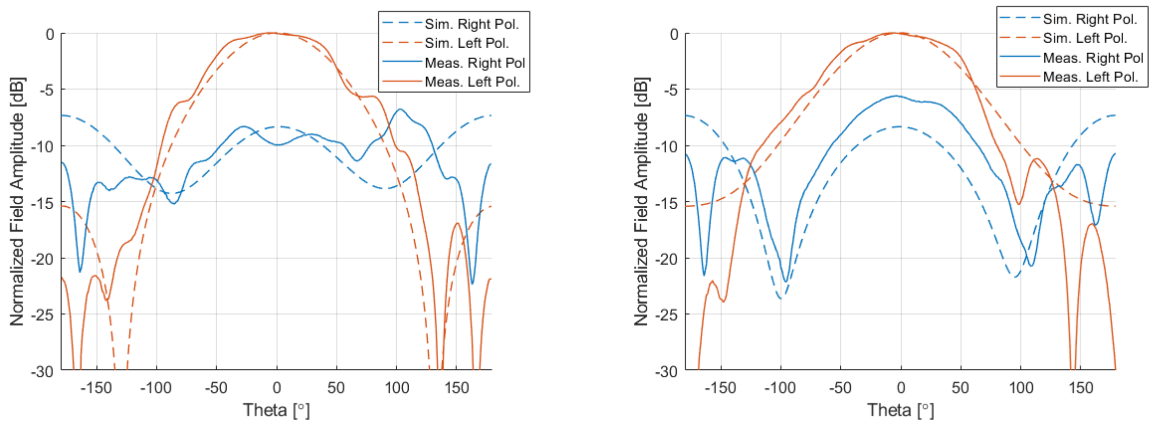

(a) **(b)**

Figure 3.12: Simulated and measured normalized radiation pattern cuts for FR-4 antenna, in free-space. (a) $\phi = 0°$. (b) $\phi = 90°$.

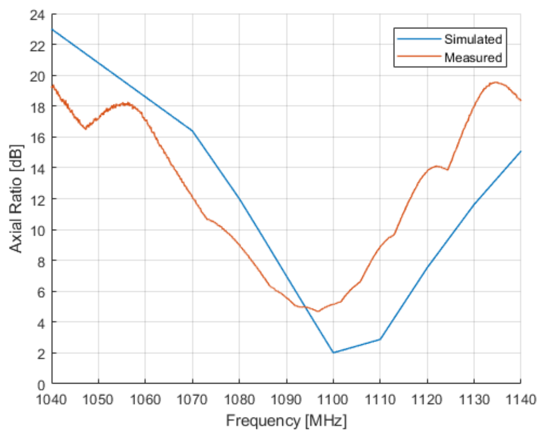

Figure 3.13: FR-4 antenna's simulated and measured values of axial ratio, for $\theta = 0°$ and $\phi = 0°$.

Efficiency

The efficiency test performed is based on the Wheeler cap method [2]. This method is based on the comparison between two impedance measurements. One, where the Antenna Under Test (AUT) is in free-space and another where the AUT is placed inside a metal cavity in order to eliminate the radiation by the antenna.

The antenna efficiency can be defined by

$$\eta = \frac{R_{rad}}{R_{rad} + R_L}, \tag{3.2}$$

where R_{rad} and R_L represent the equivalent radiation and loss resistances respectively. From the free-space measurement, the measured impedance is represented by

$$Z_{fs} = R_{rad} + R_L + jX, \tag{3.3}$$

where X is the equivalent reactance of the patch circuit model. Finally, from the measurement with the AUT inside the cap, the resulting impedance is

$$Z_{cap} = R_L + jX, \tag{3.4}$$

with all the variables defined above. Figure 3.14 represents the calculated efficiency for a frequency band from 1000 MHz to 1200 MHz.

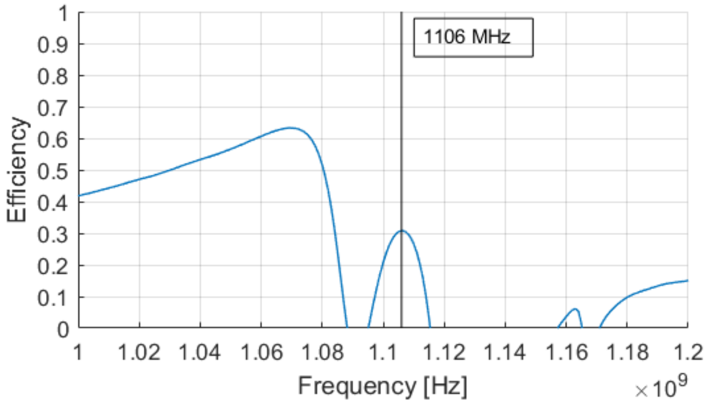

Figure 3.14: Calculated efficiency of FR-4 antenna.

It is important to note that this method is only valid for frequencies close to the resonance center frequency. At 1106 MHz, the calculated efficiency was approximately 30%. The real efficiency of the fabricated antenna will be greater or equal to 30% due to possible losses inside the cavity upon measurements.

Temperature Test

The fabricated antenna was subjected to three temperature cycles, ranging from -8 °C to 80 °C. First, the antenna was placed inside a freezer to cool down until -8 °C. Then, the reflection coefficient was quickly measured. After letting the antenna reach ambient temperature, the antenna was placed inside a PCB oven where it was heated until 80 °C. Thereafter, the antenna was removed from the oven and the reflection coefficient was again measured. The antenna's temperature was measured using a contactless infrared thermometer. Figure 3.15 shows the measured reflection coefficient of the antenna, for the ambient temperature and the highest and lowest achievable temperatures during the test.

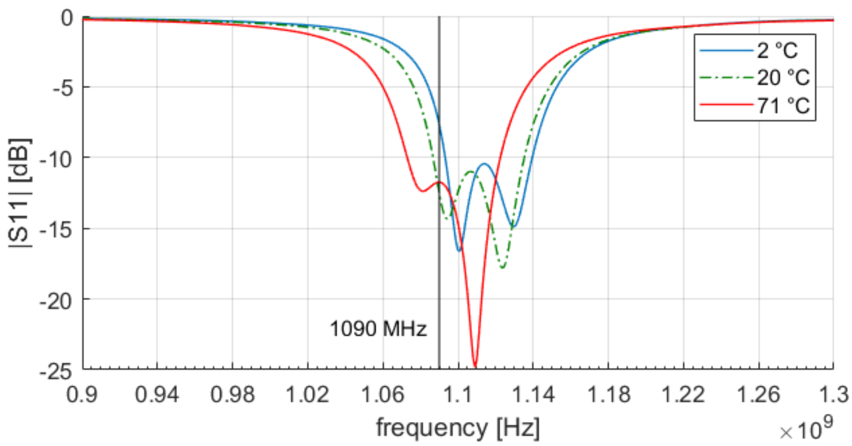

Figure 3.15: Variation of the antenna's S11 for three different temperatures.

Comparing with the ambient temperature measurement, the resonance frequency was shifted down 15 MHz, for 71 °C, and shifted up 9 MHz, for 2 °C. Considering a linear dependence of the FR-4's permittivity with temperature, the change in resonance frequency is -0.29 MHz/°C. It can be seen that when the antenna was at 2 °C, the ADS-B frequency was outside of the antenna's bandwidth.

If the material used on the final prototype has similar temperature dependence as FR-4, it would be useful to exploit the results of this test in the planning of the final prototype. As a consequence, the final antenna should be designed in such a manner that the resonance frequency is centred at 1090 MHz, for the average temperature experienced in orbit. Since this antenna has strict requirements in terms of bandwidth, the reception of ADS-B signals might be compromised for some periods during orbit, due to fluctuating antenna temperatures.

Antenna with Structure

It is important to study the performance of the antenna when integrated with the rest of the satellite. This is because, after integration, the whole satellite system is going to affect the performance of the antenna. In this section the study of the influence of the satellite's metal structure is presented.

A new model was designed and simulated, where the antenna was placed on the bottom face of the satellite's structure. The structure used in the simulation is the final model that is going to be used in the ISTsat-1. Figure 3.16 shows the model used in the simulations and the assembled prototype on a dummy structure. A dummy structure had to be fabricated, because at the time of the development of this thesis, the final ISTsat-1 structure was not yet fabricated.

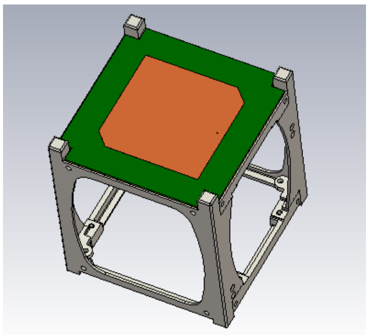

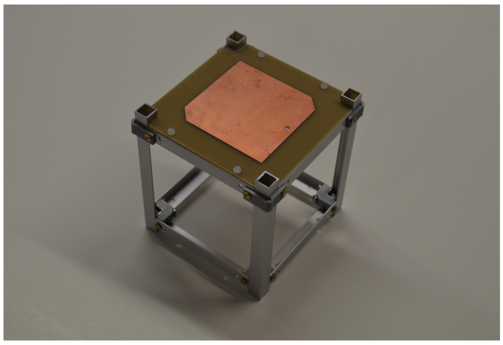

(a) (b)

Figure 3.16: FR-4 antenna integrated onto 1U CubeSat structure. (a) Simulation model. (b) Fabricated prototype.

The reflection coefficient was measured and compared to the result with the antenna in free space. Figure 3.17 shows the comparison between the reflection coefficient at the antenna's input, with and without the presence of the metal structure.

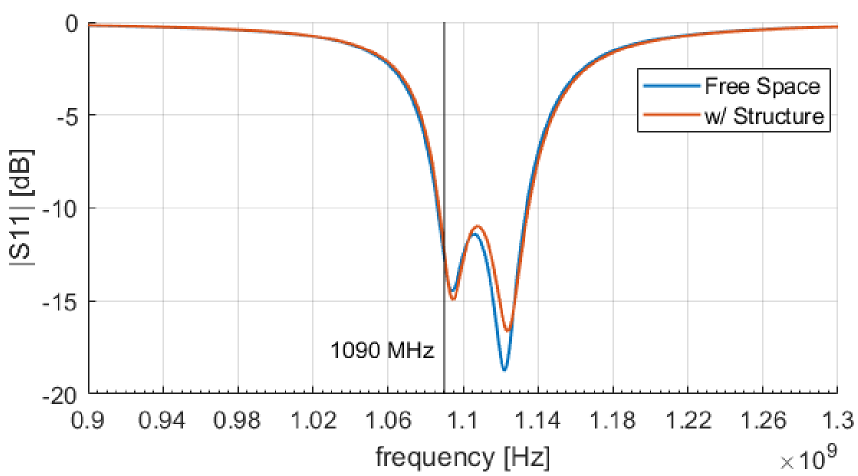

Figure 3.17: Measured S11 values for the FR-4 antenna, with and without the structure.

The variation in the reflection coefficient is minimal. It can be concluded that when integrated into the satellite's structure the antenna's impedance response remains unchanged. It was also studied the influence of the structure on the antenna's radiation pattern. Figure 3.18 shows a comparison between the simulated radiation pattern of the antenna, with and without the metallic structure.

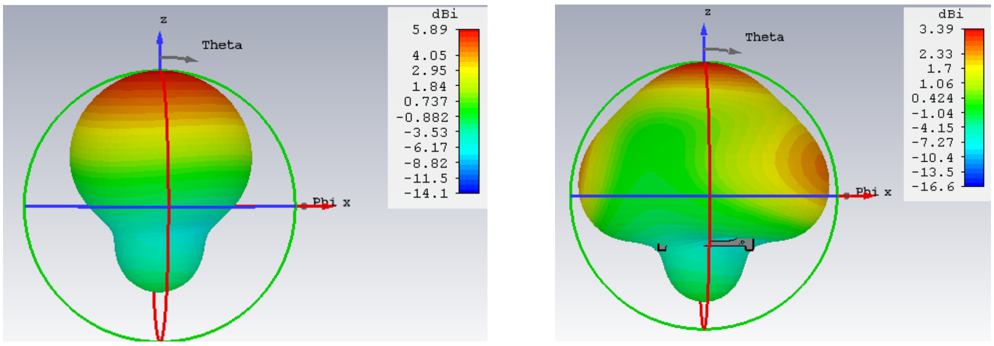

(a) **(b)**

Figure 3.18: FR-4 antenna simulated radiation pattern (directivity). (a) Antenna in free space. (b) Antenna with structure.

Observing the simulation results, it can be clearly seen that there is some power that is radiated towards the sides of the satellite. This might be due to the limited small ground plane of the antenna. This radiation pattern was also measured, and these results are illustrated on figure 3.19.

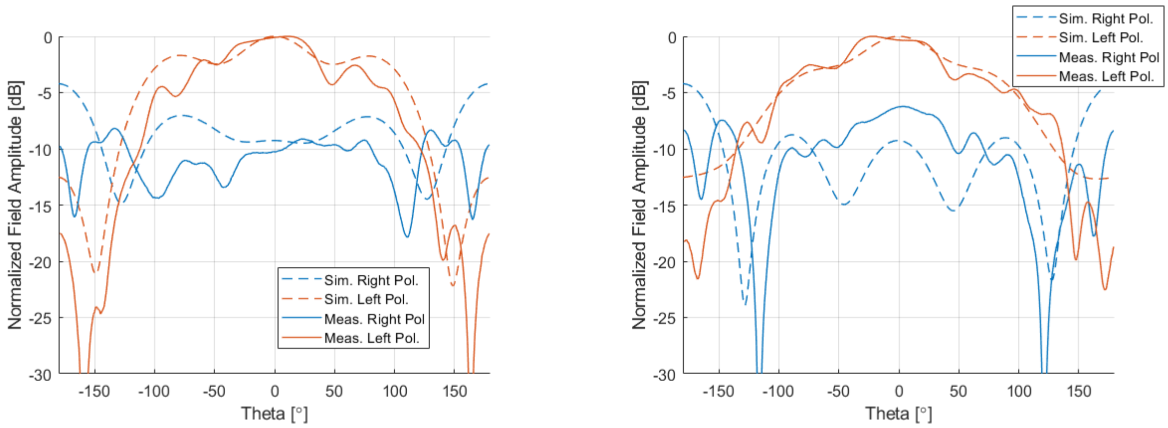

(a) **(b)**

Figure 3.19: Simulated and measured normalized radiation pattern cuts for FR-4 antenna, with the structure. (a) $\phi = 0°$. (b) $\phi = 90°$.

By analyzing the measured results, it is confirmed that when the antenna is integrated into the metallic structure, its radiation pattern is altered. It can be seen, both for $\phi = 0°$ and $\phi = 90°$ that there is power that is radiated towards the sides of the antenna, creating visible side lobes at $\theta \approx \pm 75°$. This effect is not desirable as the power that is radiated sideways is lost, degrading the link budget. The axial ratio was also measured and its results are represented on figure 3.20.

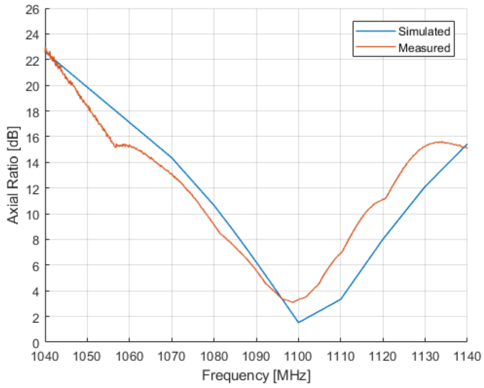

Figure 3.20: Simulated and measured values of axial ratio for $\theta = 0°$ and $\phi = 0°$, of the FR-4 antenna with structure.

The measured axial ratio is minimum at 1098 MHz, with a value of 3.1 dB. Despite being above the standard 3 dB level for circular polarization, the axial ratio improved, comparing with the results of the free space antenna.

Antenna with Structure and V/UHF Antennas

One component of the ISTsat-1 that might help the ADS-B radiation pattern is the VHF and UHF dipoles, used for TTC. These deployable metal dipoles are quite large and thus can help increase the effective ground plane of the ADS-B antenna.

A pair of V/UHF and its respective feeding circuit was developed, to study the influence of the V/UHF antennas on the ADS-B antenna radiation pattern. The ISTsat-1's "real" V/UHF antenna module is a commercial one and it wasn't available at the time of the development of this thesis. Figure 3.21 shows the simulation model and the fabricated equivalent of the FR-4 antenna integrated in the dummy structure, with the developed V/UHF antennas. On the simulation model, only the V/UHF wires were included, as it was enough to study the effects of the V/UHF antennas without increasing simulation times, by including the developed feeding circuit.

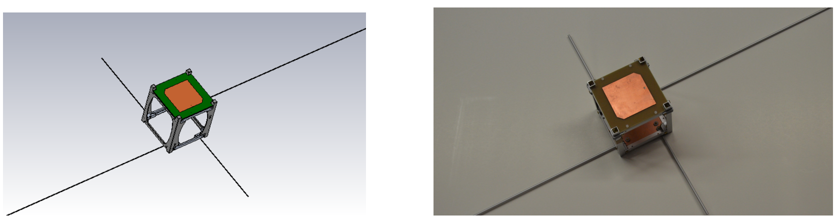

(a) **(b)**

Figure 3.21: FR-4 antenna integrated onto 1U CubeSat structure, with VHF and UHF antennas. (a) Simulation model. (b) Fabricated prototype.

The model on figure 3.21(a) was simulated and its radiation pattern is illustrated in figure 3.22.

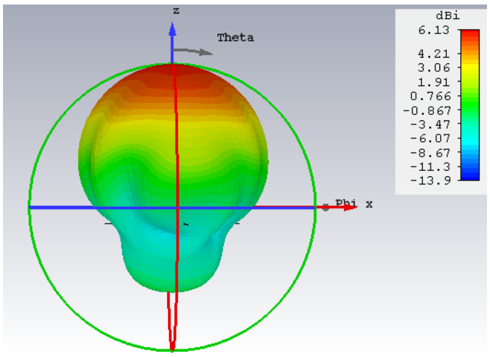

Figure 3.22: FR-4 antenna with structure and V/UHF antennas, simulated radiation pattern (directivity).

Comparing figure 3.22 to 3.18(b), the antenna's directivity increased 2.74 dB. Also, there is less power radiated towards the sides. Just like in the previous sections, the radiation pattern of the antenna with the structure and V/UHF antennas was measured and the results are represented in figure 3.23.

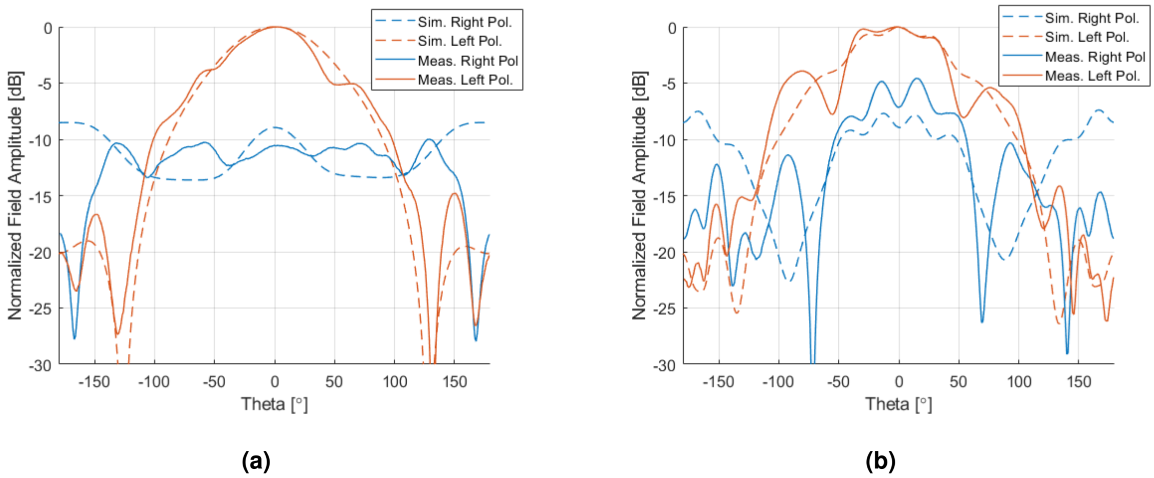

Figure 3.23: Simulated and measured normalized radiation pattern cuts for FR-4 antenna, with the structure and V/UHF antennas. (a) $\phi = 0°$. (b) $\phi = 90°$.

Looking at the left polarization field component for $\phi = 0°$, it can be seen that there is much less power radiated towards the sides, comparing with figure 3.19(a). For $\phi = 90°$, there is still some visible side lobes at ($\theta \approx \pm 75°$), but their level is lower than in figure 3.19(b). The axial ratio was also measured, in order to see if it would improve, when the V/UHF antennas are introduced. Figure 3.24 shows the simulated and measured axial ratio for the ADS-B antenna with the structure and V/UHF antennas.

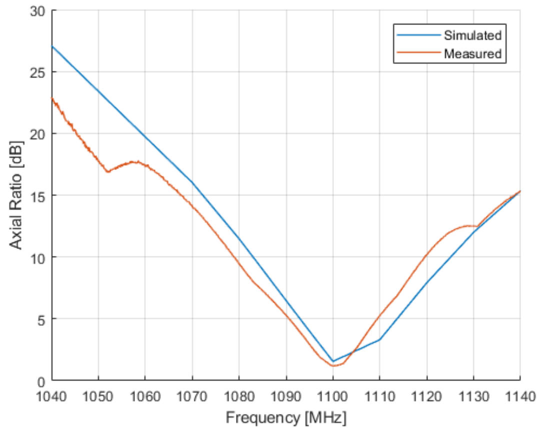

Figure 3.24: Simulated and measured values of axial ratio for $\theta = 0°$ and $\phi = 0°$, of the FR-4 antenna, with structure and V/UHF antennas.

The obtained axial ratio is quite good. The minimum is 1.2 dB at 1100 MHz and the 3 dB bandwidth is 10 MHz, centered at 1100 MHz. At the ADS-B frequency of 1090 MHz, the obtained axial ratio is 5 dB. Comparing these results with the results on figure 3.20, it is clear that the introduction of the V/UHF dipole antennas improves the ADS-B antenna's axial ratio.

Extended Ground Plane with Deployable Wires

A new solution was studied to see if the antenna's performance could be improved, in terms of gain and axial ratio. This is only a feasibility study, and will not be implemented in ISTsat-1, even if proved to work, as the inclusion of new technologies would have to be rigorously tested and space approved by ESA.

The solution consists of integrating 4 deployable metal nets, consisting of thin (1 mm diameter) metallic wires, that are folded onto the CubeSat's lateral faces, over the solar panels, during stow and launch. The wire planes, when in the stowed state, should not exceed the volume restrictions of the CubeSat standard, and the deployment mechanism has to be robust in order to prevent early deployment, inside the CubeSat deployer pod. The idea is that, after launch, the wire planes that are secured with burn wires and springs, can deploy and increase the effective ground plane of the ADS-B antenna, and thus increasing its gain and improving the radiation pattern's symmetry. In the case of a failed deployment, being very thin, the wire planes would not affect the solar panels' efficiency, while in the deployed state, they should not interfere with the VHF and UHF antennas. Figure 3.25 illustrates the simulation model and the fabricated prototype of the whole system.

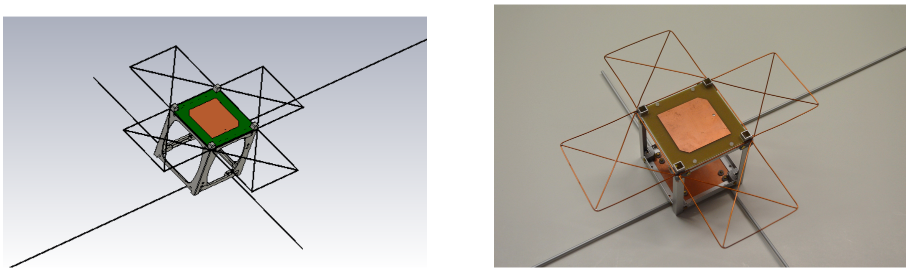

(a) **(b)**

Figure 3.25: FR-4 antenna integrated onto 1U CubeSat structure, with VHF and UHF antennas, and metallic wire planes. (a) Simulation model. (b) Fabricated prototype.

Figure 3.26 illustrates the simulated radiation pattern of this configuration.

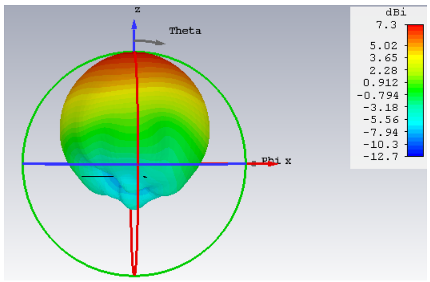

Figure 3.26: FR-4 antenna with structure, V/UHF antennas, and metal wire planes, simulated radiation pattern (directivity).

The maximum directivity obtained was 7.3 dBi, which is approximately 1.2 dB higher than the directivity obtained without the wire planes. The radiation pattern with this configuration was also measured. Such radiation pattern is represented in figure 3.27.

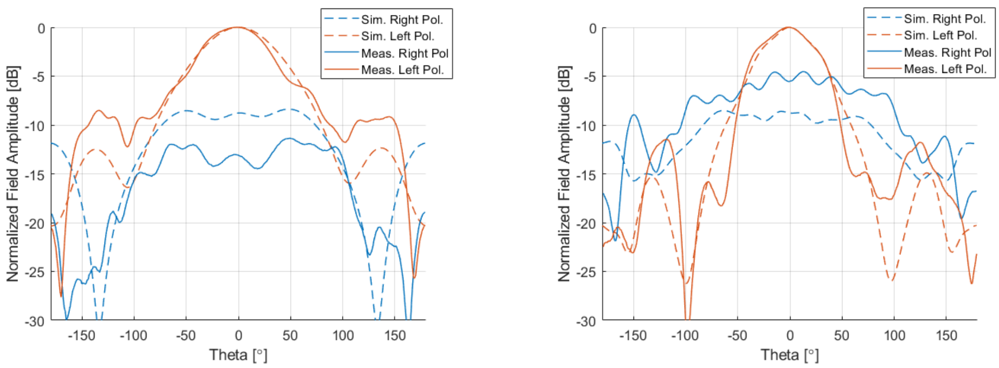

(a) **(b)**

Figure 3.27: Simulated and measured normalized radiation pattern cuts for FR-4 antenna, with the structure, V/UHF antennas and wire planes. (a) $\phi = 0°$. (b) $\phi = 90°$.

Looking at the left polarization field component, there is a well defined main beam, without visible side lobes. In the cross polarization component (right polarization), the shape of the radiation pattern is similar between measurements and simulations but the amplitude level is different. Again, this might be due to the limitations of the measurements at this frequency on our anechoic chamber. The axial ratio was again measured, and its results are presented on figure 3.28.

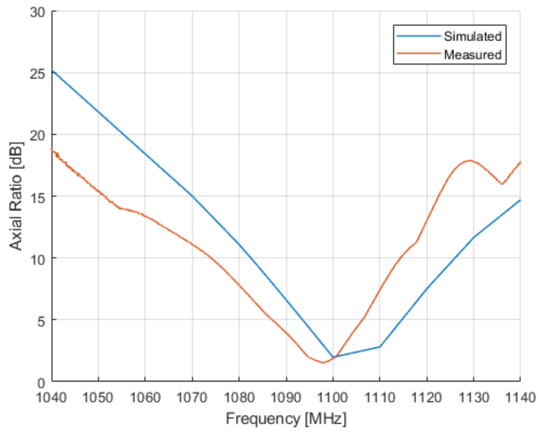

Figure 3.28: Simulated and measured values of axial ratio for $\theta = 0°$ and $\phi = 0°$, of the FR-4 antenna, with structure, V/UHF antennas and wire planes.

The results are similar to the ones of the antenna with structure and V/UHF antennas. The measured axial ratio minimum is 1.5 dB, at 1098 MHz, and a 3 dB bandwidth of 11 MHz, centered at 1098 MHz.

All the measured results of the radiation patterns were superimposed in order to have a comparison of the directivity, obtained in each configuration. These results are shown in figure 3.29.

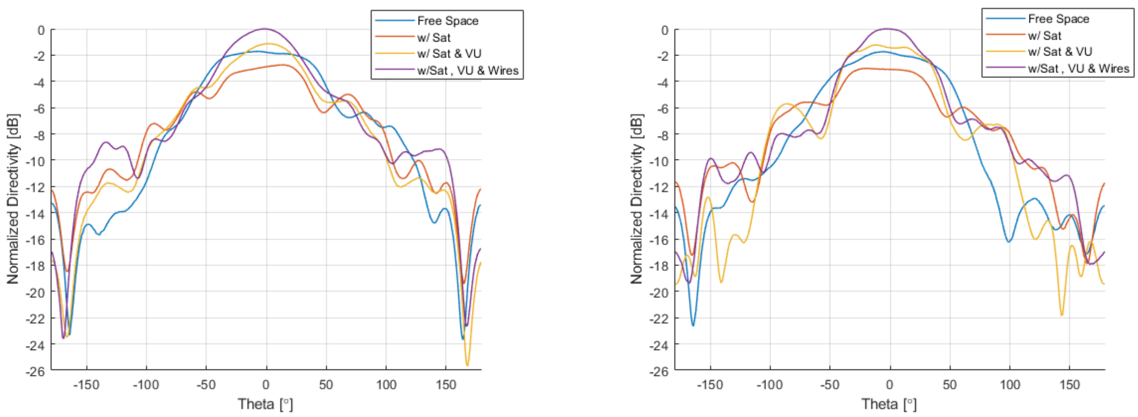

(a) **(b)**

Figure 3.29: Comparison of absolute directivity between the 4 configurations, antenna in free space, antenna with structure, antenna with structure and V/UHF antennas, and everything plus the wire planes. (a) $\phi = 0°$. (b) $\phi = 90°$.

The worst case is when the antenna is integrated into the satellite's metallic structure, the directivity drops 1.1 dB. Then, with the introduction of the VHF and UHF antennas, the antenna gains 1.8 dB. Finally, the introduction of the wire planes recover 1.1 dB more.

Concluding, the metallic wire planes come as a good solution in order to increase the overall antenna gain, but mainly for missions where the link budget is at the limit, because the achievable gain obtained with these wire planes might not justify adding four deployable planes to an already complicated CubeSat.

3.3.3 Test with ADS-B Receiver

In order to assess the performance of the developed antenna when connected to an ADS-B receiver, the antenna was connected to a commercial ADS-B receiver from uAvionix [51]. The commercial receiver was used instead of the ISTsat-1's ADS-B receiver because at the time of the development of this thesis, the ISTsat-1's ADS-B receiver was not yet fully developed nor fabricated.

Figure 3.30 illustrates the measurement setup used for the ADS-B receiver test. The antenna is secured on a tripod and connected to the ADS-B receiver, then an USB to serial converter is used to convert the messages to be read out by a computer. The software used to decode the messages is from an open source project called ArduPilot [52], and the tool used is the mavlogdump, for the mavlink [53].

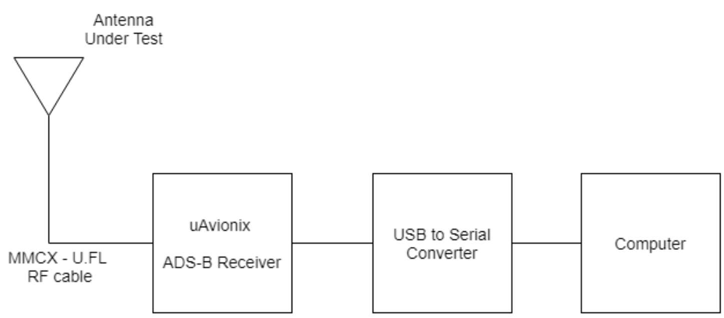

Figure 3.30: Diagram of the ADS-B test setup.

The measurements were made at the 12th floor of IST's north tower in Lisbon, in order to favour the line of sight between the airplanes and the antenna. After some preliminary tests it was confirmed that the direction that resulted in best results, meaning more plane signals acquired, was the SW direction. The difference in acquired signals with different antenna rotation angles was also tested. The three different antenna rotation angles are represented in figure 3.31.

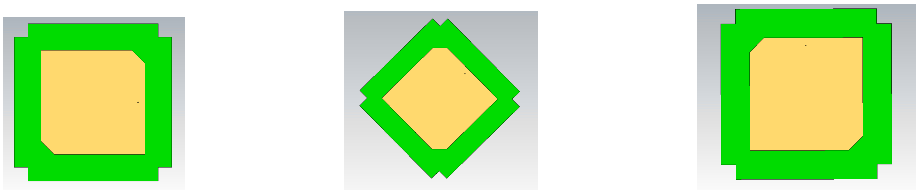

(a) **(b)** **(c)**

Figure 3.31: Antenna rotation angles used for ADS-B test: (a) 0°, (b) 45°, (c) 90°.

This rotation test is important because the fabricated antenna is not circularly but elliptically polarized, due to the shift in the resonance frequency. The antenna's rotation angle that led to the best results was 90°. Figure 3.32 illustrates the results from the ADS-B measurements during 1 hour, with the antenna at 90°, and figure 3.33 shows all the airplanes' position in the area, transmitting ADS-B signals, in the beginning of the measurement period.

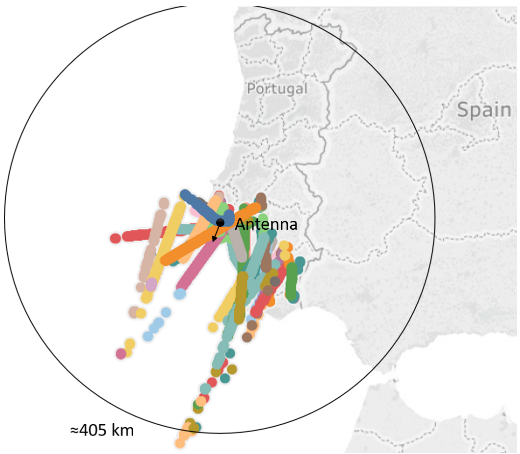

Figure 3.32: Airplane signals received with FR-4 antenna, during 1 hour of measurements.

Figure 3.33: Airplanes transmitting ADS-B, over the Iberian Peninsula and Morocco. Data from flightradar24 [54].

It can be seen by the distribution of the airplane signals in figure 3.32, that the fabricated antenna is directional. The range of the setup (antenna with receiver) is approximately 405 km. The message error rate was calculated because, although it is optimal to obtain the 400 km of range, the number of received and correctly decoded airplane signals is also important to evaluate the performance of the ADS-B receiving chain. Two types of errors were considered. One, where all the messages not containing the airplanes' coordinates was considered an erroneous message. Another, where it was considered an erroneous message when there were no coordinates nor callsign. The message error rate was 19.5% for the first case, and 26.8% for the second.

3.4 Final Antenna Prototype

The substrate material chosen for the final prototype is RT/duroid® 6010, with relative electric permittivity of 10.5. This high permittivity, ceramic-PTFE substrate, has tight ϵ_r and thickness control, low moisture absorption, good thermal mechanical stability, and low outgassing properties, which make it a good choice for space applications.

3.4.1 Simulations and Measurements

This antenna follows the same design as the pre-prototype, being a square patch with truncated corners. A substrate thickness of 2.5 mm was chosen as the best compromise between high efficiency and low bandwidth. Figure 3.34 illustrates the designed 3D antenna model and the respective fabricated prototype. The antenna's parameters are specified in table 3.3.

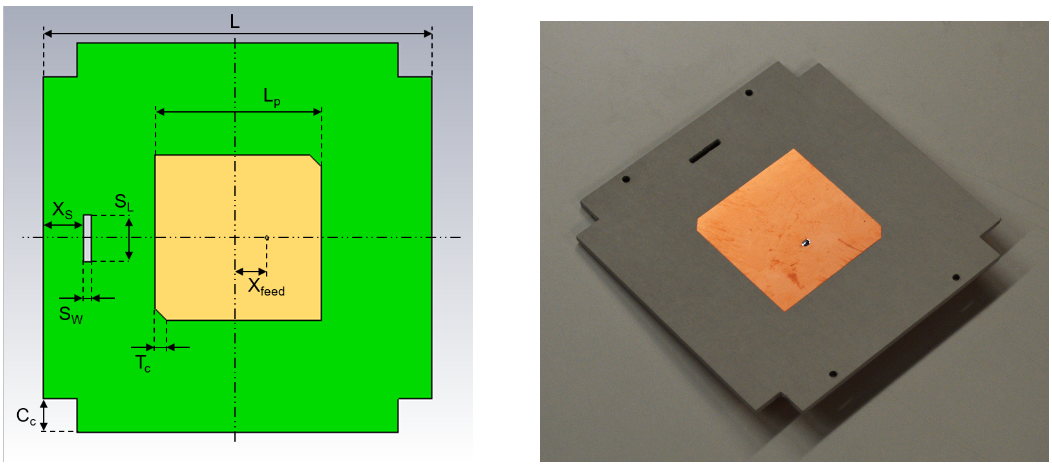

(a) **(b)**

Figure 3.34: Patch antenna with RT6010 substrate. (a) Simulation model. (b) Fabricated prototype.

Table 3.3: RT6010 patch antenna dimensions in millimeters.

L	L_p	X_{feed}	T_c	C_c	X_S	S_L	S_W
98	41.74	7.3	2.97	8.5	10.1	11.8	1.95

A small slot had to be opened at the edge of the antenna (see figure 4) to allow temporary servicing access to other internal sub-systems after complete system assembling. This is a small slot compared to one wavelength, and therefore the radiation through the slot is minimal and does not affect the sub-systems that will be mounted below the antenna. The antenna's reflection coefficient was measured and the results are represented in figure 3.35.

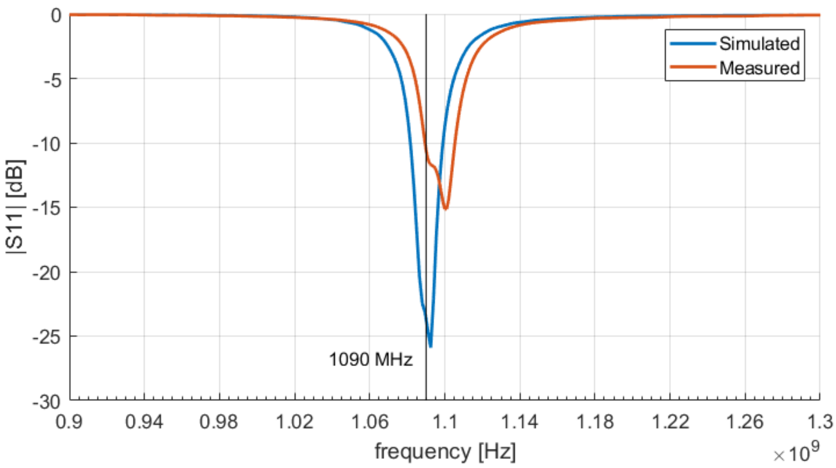

Figure 3.35: Comparison between simulated and measured reflection coefficients.

The center resonance frequency of the fabricated prototype is 1095 MHz, which is 5 MHz (0.5% error) up-shifted, comparing with the simulated result. This error is due to the small but present 2.5% uncertainty, on the electric permittivity value. This shift in frequency is not detrimental to the good performance of the antenna. In this case it is actually desirable, as the expected antenna temperature in orbit is well below room temperature, which means that at nominal antenna temperature (0 °C), the resonance frequency will be centered at around 1090 MHz. The obtained bandwidth is 17 MHz and 16 MHz, for the simulated and fabricated antenna, respectively.

In regards to this antenna's radiation pattern, it is expected that the gain will be higher than the FR-4 antenna. Figure 3.36 illustrates the simulated antenna radiation pattern, at the center resonance frequency.

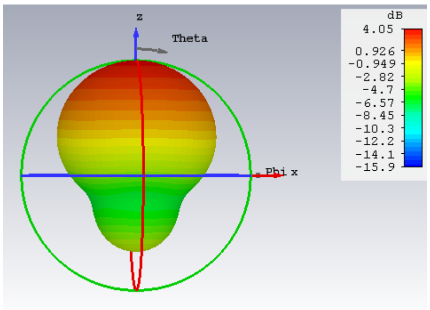

Figure 3.36: RT6010 in free-space, simulated radiation pattern (gain).

The obtained antenna gain is approximately 4 dB. This is a good result for such compact antenna, as with a higher gain there is a bigger margin when the gain is reduced by the influence of the Cube-Sat, comparing to the FR-4 prototype. Figure 3.37 shows the measurement setup for measuring the antenna's radiation pattern, and figure 3.38 illustrates the measured and simulated radiation pattern cuts.

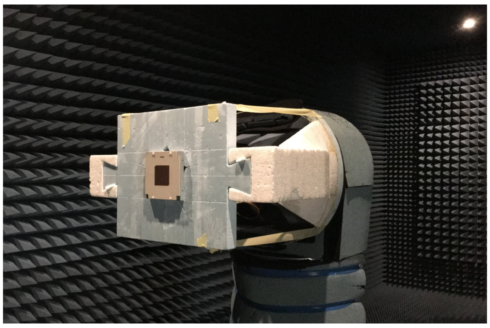

Figure 3.37: RT6010 antenna mounted on a positioner, inside the anechoic chamber.

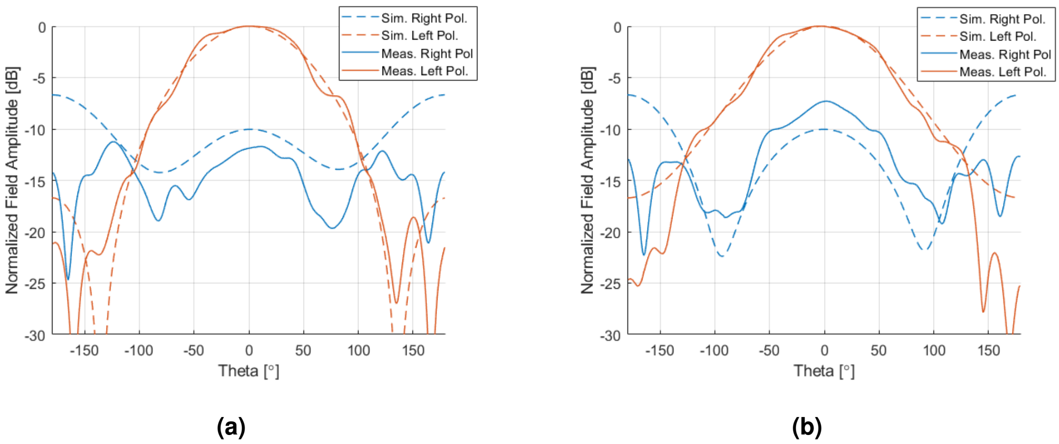

Figure 3.38: Simulated and measured normalized radiation pattern cuts for RT6010 antenna, in free-space. (a) $\phi = 0°$. (b) $\phi = 90°$.

There is good agreement between simulated and measured results. Again, probably due to the limitations of the anechoic chamber, there is a small difference in the cross-polarization component, between measurements and simulations. The axial ratio was also measured and is represented in figure 3.39.

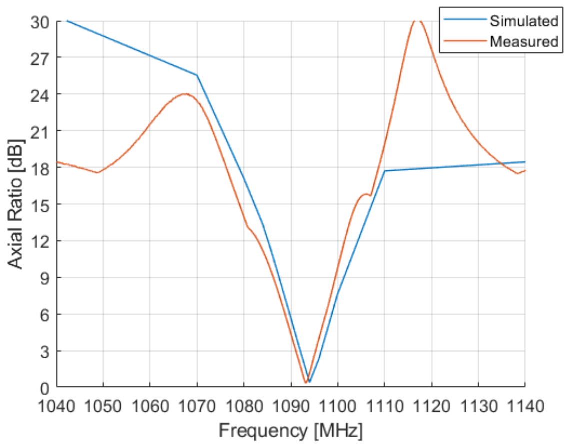

Figure 3.39: RT6010 antenna's simulated and measured values of axial ratio, for $\theta = 0°$ and $\phi = 0°$.

The measured axial ratio is low, being 0.33 dB at 1093 MHz. This is a good result, which means that the antenna has almost pure circular polarization. The axial ratio bandwidth is approximately 4 MHz, around 1093 MHz.

Efficiency

The method used to measure and calculate the efficiency of the antenna is the same as described in section 3.3.2. Figure 3.40 shows the calculated efficiency of the RT6010 antenna.

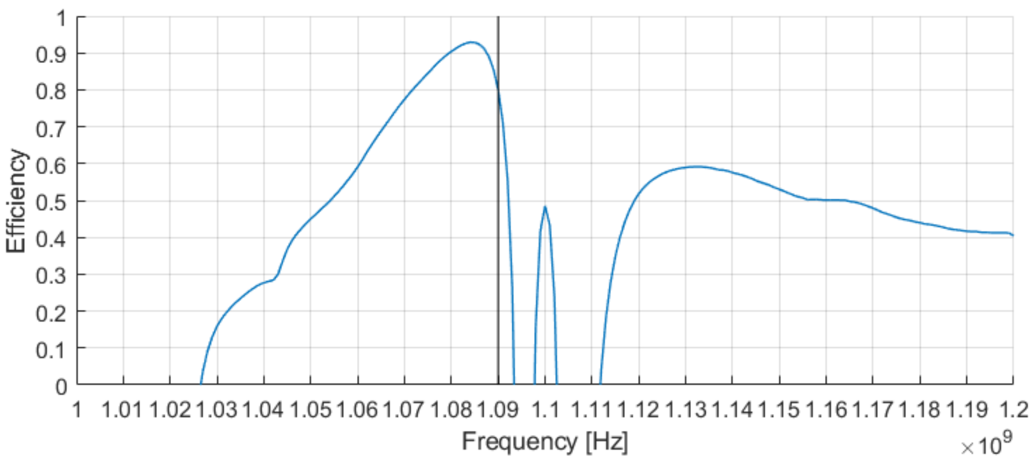

Figure 3.40: Calculated efficiency of RT6010 antenna.

The calculated efficiency at 1090 MHz is approximately 80%. This value is much higher than the efficiency of the FR-4 prototype, hence the higher realized gain.

Temperature Test

The temperature tests made to the RT6010 antenna are identical to the ones described in section 3.3.2. The antenna's reflection coefficient was measured at three different temperatures: cold, room temperature, and hot measurements. Figure 3.41 illustrates these results.

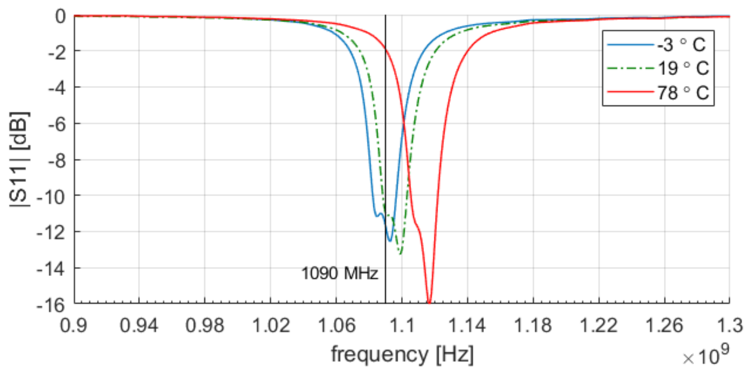

Figure 3.41: Variation of the antenna's S11 for three different temperatures.

When the antenna was cooled to -3 °C, its resonance frequency shifted down 6 MHz, and shifted up 18 MHz when it was heated to 78 °C, comparing to the room temperature measurement. This resonance frequency shift, translates into a resonance frequency change per degree of 0.298 MHz/°C. In order to see what was the antenna's operational temperature range in terms of bandwidth, the reflection coefficient curve for 19 °C was extrapolated, using the frequency variation of 0.298 MHz/°C. Figure 3.42 shows the antenna's reflection coefficient for the minimum and maximum temperatures that result in the ADS-B frequency of 1090 MHz still being within the bandwidth.

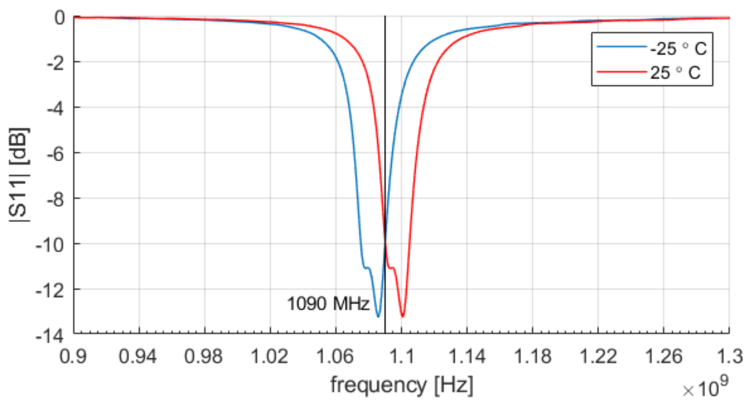

Figure 3.42: Antenna's S11 for minimum and maximum operational temperatures.

The resulting minimum and maximum operational temperatures, so that the ADS-B frequency is inside the antenna's bandwidth, are -25 °C and 25 °C, respectively. This is a wide enough temperature range, that accommodates the expected antenna's temperature in orbit.

Antenna with Structure

As with the FR-4 antenna, the RT6010 antenna was integrated in the fabricated 1U CubeSat structure. Figure 3.43 illustrates the fabricated prototype, integrated into the CubeSat structure.

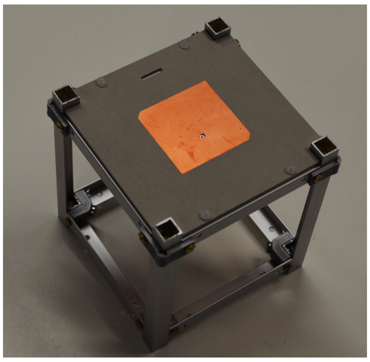

Figure 3.43: Final antenna prototype, integrated onto CubeSat structure.

It has been shown in section 3.3.2 that the inclusion of the CubeSat's metallic structure does not alter the antenna's resonance frequency. Considering this, the antenna's reflection coefficient, when integrated onto the structure, will not be represented here. Regarding the radiation pattern, figure 3.44 shows the simulated radiation pattern.

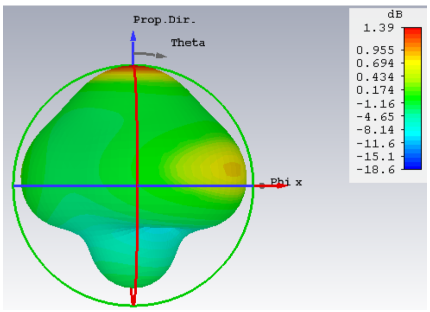

Figure 3.44: RT6010 antenna with structure, simulated radiation pattern (gain).

Just like with the FR-4 antenna, the gain of the RT6010 antenna, decreases when integrated onto the CubeSat structure. There is a decrease of approximately 2.5 dB in gain. Also, it can be seen that more power is radiated towards the side of the antenna, comparing to the free-space antenna's radiation pattern. The measured radiation pattern was compared to the simulated one and is illustrated in figure 3.45.

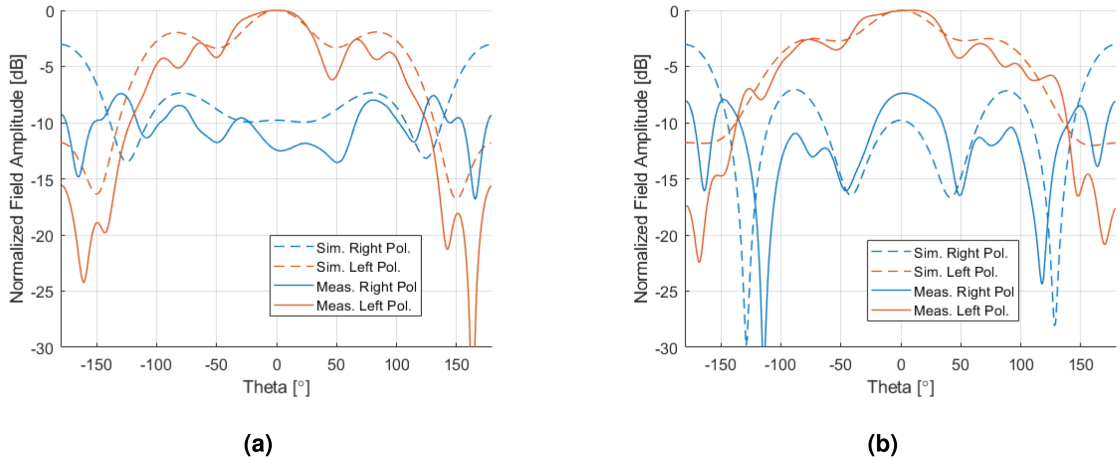

Figure 3.45: Simulated and measured normalized radiation pattern cuts for RT6010 antenna, with the structure. (a) $\phi = 0°$. (b) $\phi = 90°$.

Within the measurements limitations, there is a good agreement between simulated and measured results. Again, there are visible side lobes at $\theta \approx \pm 75°$. The axial ratio was also measured and is represented in figure 3.46.

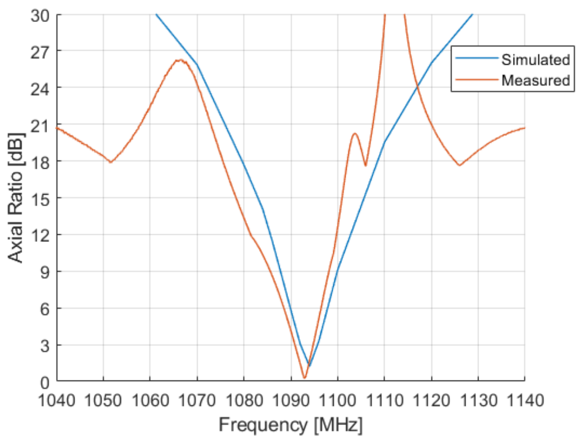

Figure 3.46: Simulated and measured values of axial ratio for $\theta = 0°$ and $\phi = 0°$, of the RT6010 antenna with structure.

The measured axial ratio is minimum at 1093 MHz, with a value of 0.22 dB, and a 3 dB bandwidth of 4 MHz. These are good and mean that the CubeSat structure has little to no influence on the antenna's circular polarization.

Antenna with Structure and V/UHF Antennas

The final configuration consists of the RT6010 antenna integrated onto the CubeSat structure, with the V/UHF antennas mounted on the opposite face. Figure 3.47 shows the fabricated prototype.

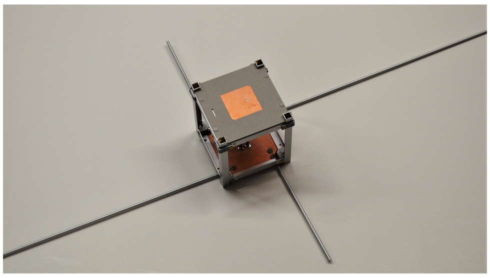

Figure 3.47: Final antenna prototype, integrated onto CubeSat structure, with V/UHF antennas.

The simulated radiation pattern is presented in figure 3.48.

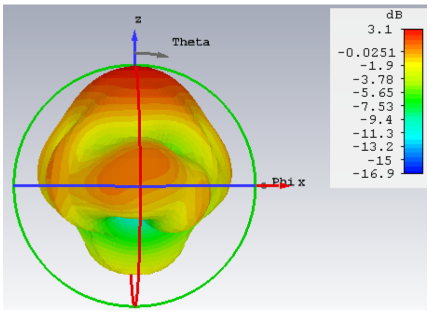

Figure 3.48: RT6010 antenna with structure and V/UHF antennas, simulated radiation pattern (gain).

The gain obtained is 3.1 dB, which is approximately 1.5 dB higher than without the V/UHF antennas. This is a very good result, as is well above the required 0 dB of gain, specified in section 3.1.1. Figure 3.49 shows the antenna setup used to measure the radiation pattern. The comparison between simulated and measured radiation patterns is illustrated in figure 3.50.

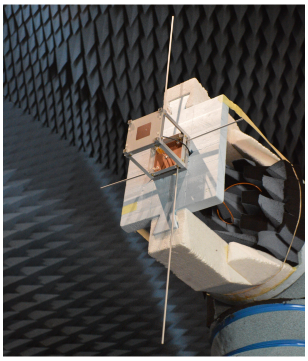

Figure 3.49: RT6010 antenna with structure and V/UHF antennas, mounted on a positioner inside the anechoic chamber.

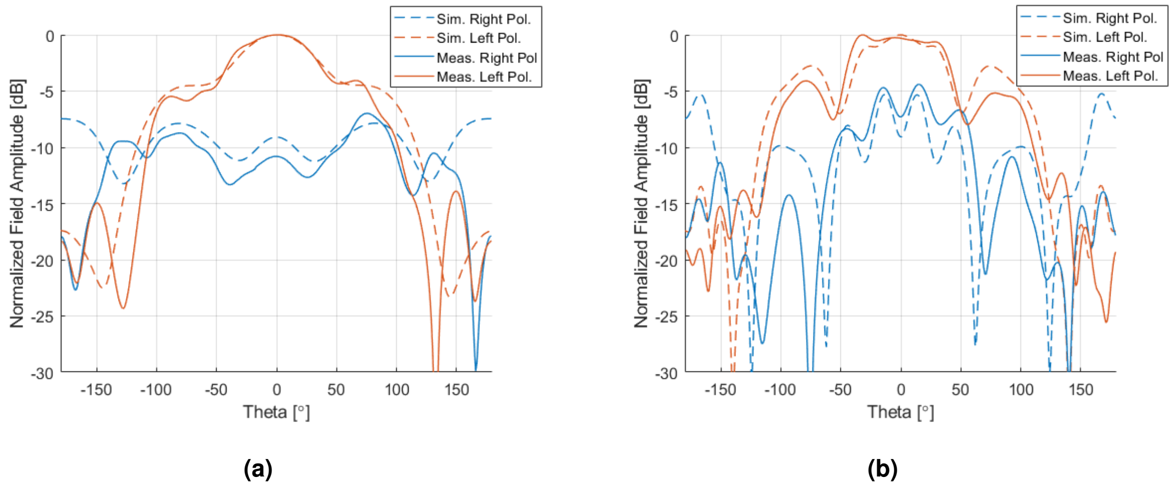

Figure 3.50: Simulated and measured normalized radiation pattern cuts for RT6010 antenna, with the structure and V/UHF antennas. (a) $\phi = 0°$. (b) $\phi = 90°$.

There is a very good agreement between simulation and measurements. With this in mind, the simulated results are validated by the measurements, and the actual antenna gain should be approximately the same as the simulated result. Figure 3.51 shows the comparison between simulated and measured axial ratio.

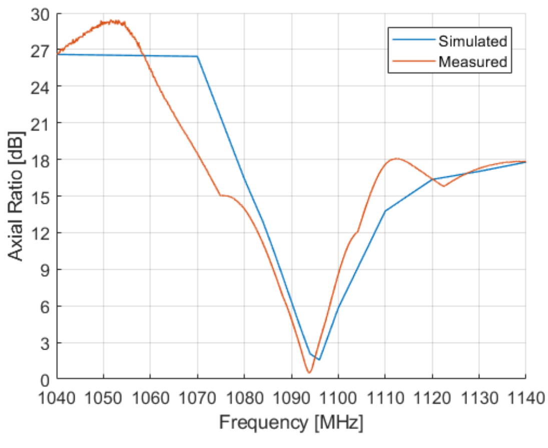

Figure 3.51: Simulated and measured values of axial ratio for $\theta = 0°$ and $\phi = 0°$, of the RT6010 antenna with structure and V/UHF antennas.

The axial ratio of the antenna integrated onto the satellite, with the V/UHF antennas, is quite low at 0.5 dB, for 1094 MHz. The 3 dB axial ratio bandwidth is identical to the previous cases, being 4 MHz centered at 1094 MHz. It can be concluded that, the antenna's axial ratio is unaffected, by the inclusion of the CubeSat structure and the V/UHF antennas.

3.4.2 Test with ADS-B Receiver

The developed final-prototype was subjected to a ADS-B system test, identical to the one specified in section 3.3.3. For this antenna, the antenna rotation that was used, was 0°. Any antenna rotation could have been used, as the antenna is circularly polarized, close to resonance frequency. The tests were carried out from the same location, and for the same duration, as the FR-4 antenna's ADS-B tests. Figure 3.52 shows the setup used to receive the ADS-B signals.

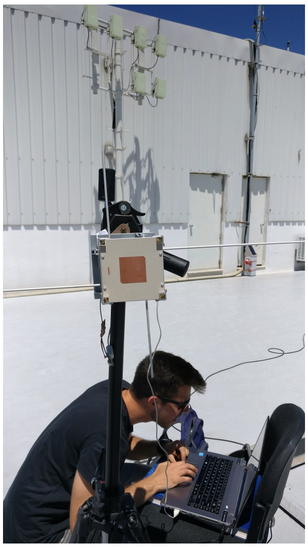

Figure 3.52: ADS-B test setup, with the ADS-B antenna and V/UHF antennas mounted onto the structure.

Antenna in Free Space

Figure 3.53 illustrates the position of the airplanes, retrieved from the ADS-B signals received with the antenna.

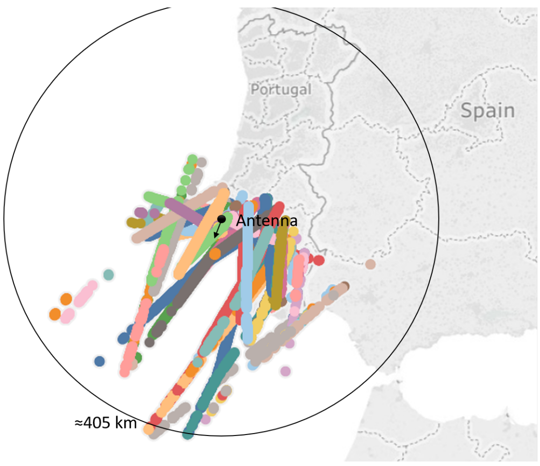

Figure 3.53: Airplane signals received with RT6010 antenna, during 1 hour of measurements.

The results corroborate the directional radiation pattern of the antenna. The range obtained with this antenna is identical to the one obtained with the FR-4 pre-prototype. A possibility for this, is that the link-budget is not very dependent on the antenna's gain, as the receiver used has relatively low sensitivity (-84 dBm). In this case, the limitation might be the attenuation from the horizon, as for distances greater than 400 km, with an airplane traveling at 10 km of altitude, the line of sight is blocked by the horizon. The RT6010 antenna did however receive almost double the amount of airplane signals, 99449 comparing to the 57289 of the FR-4 prototype. The message error rate was 17.7%, for no information on position, and 23.6%, for no information on position nor callsign.

Antenna with Structure

Figure 3.54 shows the position of the airplanes, retrieved from the ADS-B signals received with the antenna integrated onto the CubeSat structure.

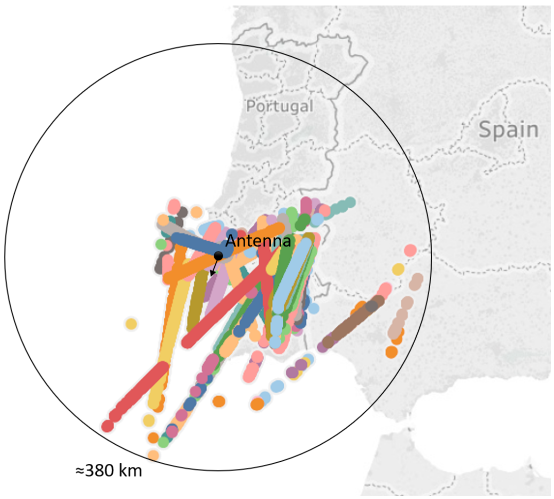

Figure 3.54: Airplane signals received with RT6010 antenna on the structure, during 1 hour of measurements.

Comparing these results to the ones on figure 3.53, the range has decreased from 405 km to 380 km. This small decrease in range is within the measurement error, as the range calculation was made manually and it is only an estimate. What is noticeable is that both error rates increased. They are now, 22.1% and 29.6%, for the first and second error cases, respectively.

Antenna with Structure and V/UHF Antennas

Figure 3.55 shows the position of the airplanes, retrieved from the ADS-B signals received with the antenna integrated onto the CubeSat structure, with the VHF and UHF antennas.

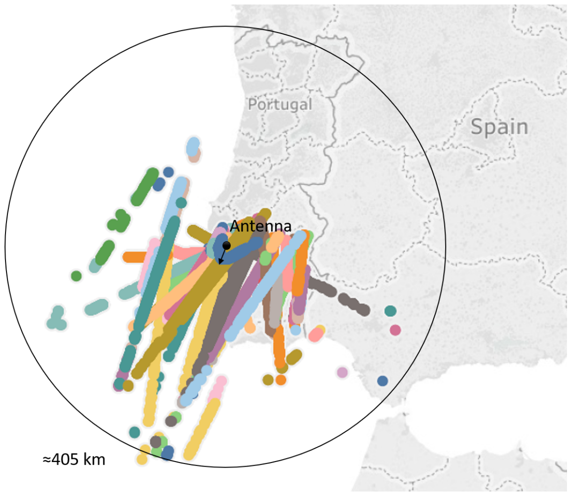

Figure 3.55: Airplane signals received with RT6010 antenna on the structure, with VHF and UHF antennas, during 1 hour of measurements.

Again, the approximate range obtained with this setup is very good, at around 405 km. The range is still limited by the attenuation introduced by the curvature of the Earth, which will not be present when the satellite will be in orbit. Without this attenuation, it is expected that the range will be closer to the desired 600 km. The message error rate improved, comparing to the case presented above, with 18.6% and 22.7%, for the first and second error cases, respectively.

4

CubeSat Reflect Array Antenna

Contents

CubeSat Reflect Array Antenna

4.1 System Analysis

The objective of the development of this RA antenna, was to provide a circularly polarized, high gain antenna solution for the Ka uplink band (27 - 31 GHz), that can be integrated into a 1U CubeSat, for fast mobile broadband access applications. The high gain is needed to compensate for the low power transceivers used for such applications, and also to allow for higher throughput rates. When used for a specific application there should always be a link-budget study, like the one presented in the previous chapter, to understand the necessary antenna gain for a good communication link. The achievable antenna gain is limited by its aperture size and thus there are some challenges when integrating high gain antennas into the small CubeSat structure. With this in mind, a deployable RA antenna that fits into a 1U CubeSat, was developed and fabricated. For this antenna the restriction of not wanting a deployable solution does not apply, as this antenna is not meant to be launched in the immediate future.

The best position to mount a deployable RA antenna on a 1U CubeSat, was found to be the satellite's (nadir) bottom face. This presents itself as the best position due to the side and top faces being usually covered with solar panels. The developed antenna will be integrated on the bottom side of the satellite and will have an aperture area of 10 x 10 cm^2, which corresponds to the bottom face area. The feed antenna for the RA will also be mounted on the bottom face, illuminating the RA aperture. The main idea is that the RA surface can be folded onto the bottom face, over the feed, during stow and launch. When in orbit, the RA surface which is secured by a burn wire and springs at the hinges, will be released and deployed to its operating state. Figure 4.1 illustrates the general idea for this RA system, integrated on a 1U CubeSat.

The maximum theoretical directivity of an aperture antenna can be defined by

$$D_{max} = \frac{4\pi A_{ap}}{\lambda^2} sin(\alpha), \tag{4.1}$$

where A_{ap} is the aperture area, λ the wavelength and α the angle of the outgoing wave, radiated by the aperture, with the surface normal. Considering the available space of 10 x 10 cm^2, the wavelength

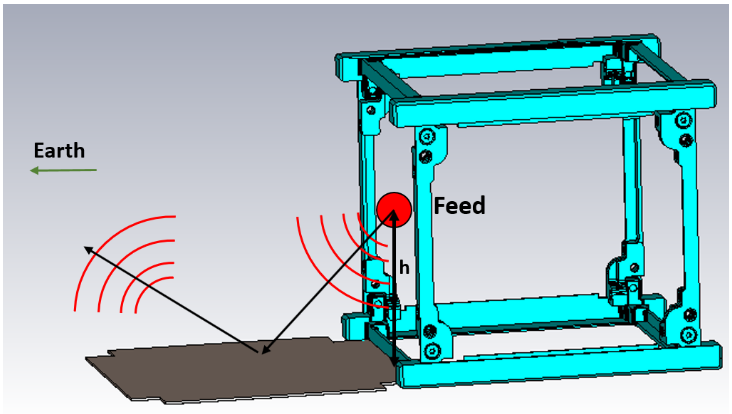

Figure 4.1: Reflectarray antenna system in the deployed position, integrated on the bottom face of a 1U CubeSat structure.

of 1 cm (f = 30 GHz), and an angle of 45° for the output beam, the maximum theoretical directivity is 29.5 dB. The output angle was chosen as 45°, because it is halfway between the normal and tangential directions, while still pointing at the Earth, for an orbit of 400 km of altitude. Considering a -3dB beamwidth of 8° and -10 dB beamwidth of 14°, the approximated ground coverage diameter would be 56 km and 200 km, respectively, for an orbit at 400 km of altitude.

4.2 Phase Distribution

As stated in 2.3.1, in order to achieve beam collimation, the RA must introduce the necessary phase shift. This phase shift cannot be implemented in a continuous manner throughout the surface, as the use of unit cells imply a spacial discretization of the phase. Smaller unit cells will allow for a better discretization. Usually, as a rule of thumb, the size of the unit cells should be smaller than one wavelength. Figure 4.2 illustrates a generic RA system, with a feed and an arbitrary number of cells.

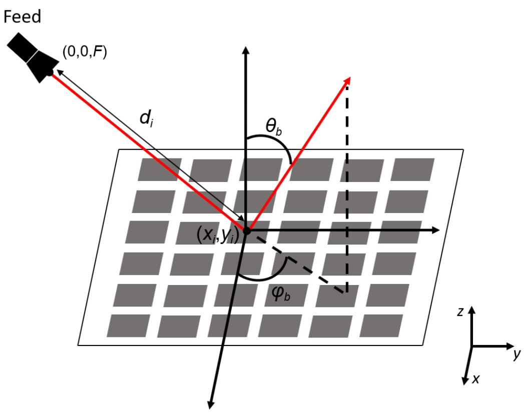

Figure 4.2: Reflect array antenna diagram, with offset feed.

In order to obtain a beam with a certain tilt angle of (θ_i, ϕ_i), the phase distribution must be

$$\Phi(x_i, y_i) = -k_0[sin(\theta_b)cos(\phi_b)x_i - sin(\theta_b)sin(\phi_b)y_i], \tag{4.2}$$

where k_0 is the free space wavenumber, and (x_i, y_i) a point in the aperture surface. In the case of the RA, the unit cells must introduce a phase shift that accounts for the different path lengths between the feed and each cell. The phase at the RA surface, after reflection of the beam, can be defined by

$$\Phi(x_i, y_i) = -k_0 d_i + \Phi_{uc}(x_i, y_i), \tag{4.3}$$

where d_i is the distance between the feed phase center and each unit cell, and $\Phi_{uc}(x_i, y_i)$ the phase shift introduced by each unit cell. After equating equation 4.3 to 4.2 and choosing ϕ_i = 0°, for this specific RA antenna system, the needed phase shift that each cell must induce is defined by

$$\Phi_{uc}(x_i, y_i) = k_0 d_i - k_0 x_i sin(\theta_b). \tag{4.4}$$

It was chosen a feed height of h = 50 mm, positioned at the border of the RA, with an input and output beam angle of 45°. The necessary phase distribution can be calculated with equation 4.4, and is represented in figure 4.3.

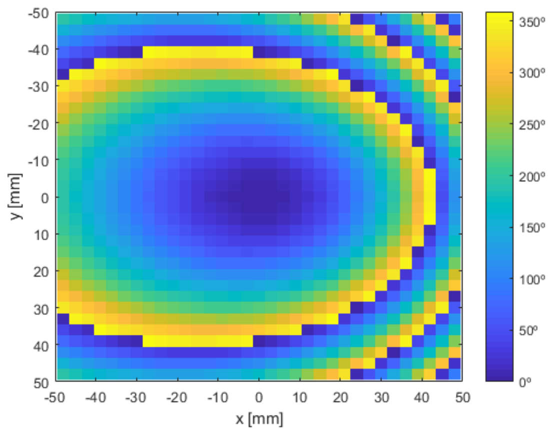

Figure 4.3: Necessary phase shift to achieve beam collimation. Each pixel represents one 3 x 3 mm^2 unit cell.

In the next section, the unit cell design to achieve the necessary phase shift, is presented.

4.3 Reflect Array Preliminary Simulations

A first approximation of the antenna's directivity and radiation pattern was obtained using a hybrid geometrical optics/physical optics tool, called KH3D [55]. This tool calculates the radiation pattern of an arbitrary aperture, by considering the amplitude and phase of the tangential field component at the aperture surface, originated from the feed. The use of this tool allows easy optimization of the RA system, in terms of feed position and gain, as this method is quite light regarding computational power, compared to the full-wave simulations that are required in a later development phase. Good results were obtained when h = 50 mm, with the feed pointing towards the centre of the RA surface, with gain of 11 dB and a -3 dB beamwidth of 33°. The feed gain of 11 dB was chosen as a compromise between energy spillover and uniform illumination. Figure 4.4 shows the amplitude and phase of the tangential field component at the aperture surface.

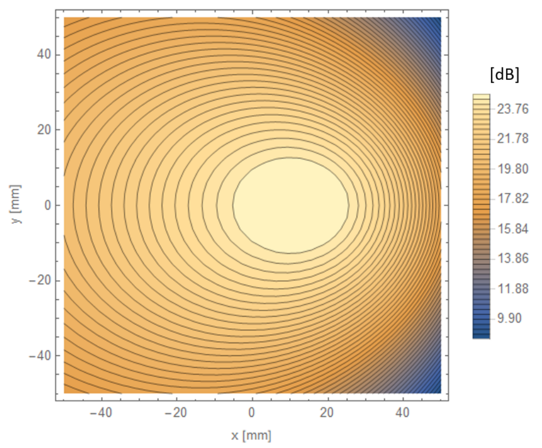

(a)

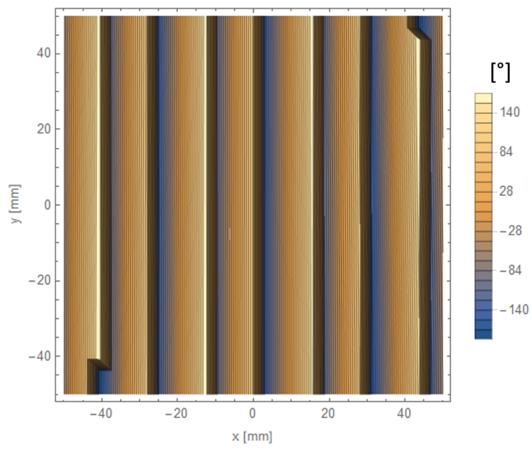

(b)

Figure 4.4: Distribution of the field at the aperture. (a) Amplitude. (b) Phase.

The resulting aperture illumination is quite uniform, but the amplitude at the left edge of the aperture is still quite large, compared to the maximum amplitude value. This will probably introduce noticeable side lobes in the RA radiation pattern. The calculated radiation pattern is illustrated in figure 4.5.

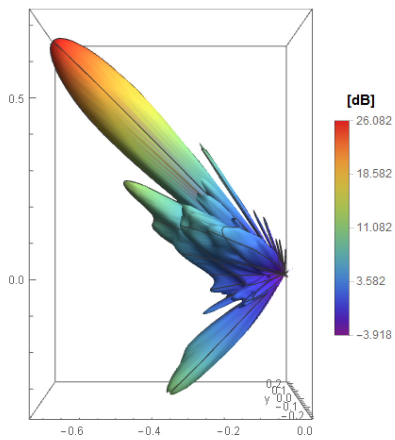

Figure 4.5: Calculated radiation pattern of 10 x 10 cm^2 reflectarray.

There is a well defined beam with 45° of tilt and approximately 26.1 dB of directivity. Considering the maximum theoretical directivity of 29.5 dB, the resulting theoretical aperture efficiency is approximately 45.7%.

4.4 Unit Cell Design

The unit cells designed for this RA antenna consist of two concentric square ring resonators. This unit cell design proved to be a good option for this application, as the obtained phase shift at 30 GHz covered the whole 0° to 360° range. The unit cell is 3 x 3 mm^2 and the phase shift is obtained by varying the outer ring resonator's side length, and consequently the inner ring side length as well. Figure 4.6 illustrates one unit cell with a specific outer ring side length, and its parameters are specified in table 4.1.

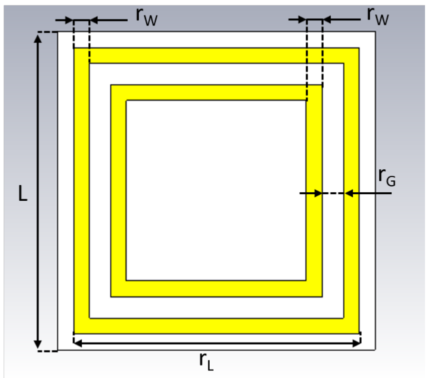

Figure 4.6: Unit cell geometry.

Table 4.1: Unit cell dimension parameters in millimeters.

L	r_W	r_G
3	0.15	0.2

The substrate used for these unit cells was RT/duroid® 5880, with a thickness of 0.787 mm, ϵ_r = 2.2 and tan δ = 0.0009. This is a space rated substrate with low outgassing properties, low thermal coefficients and quite low losses.

The unit cells were simulated and optimized by full-wave analysis using CST-MWS [1], with the frequency domain solver. In order to reduce the simulation and optimization time, the scattering matrix was obtained for an infinite periodic structure of the same unit cell. This stands as a good approximation when designing unit cells, to obtain the introduced phase shift with the change of a design parameter. Figure 4.7 shows the reflection coefficient for these unit cells for different values of r_L, between 1.1 and 2.7 mm.

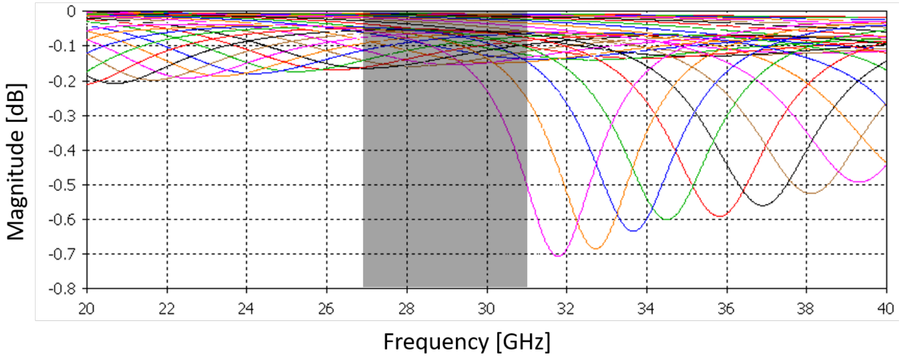

Figure 4.7: S11 magnitude of the designed unit cell. Each color represents a different outer ring length.

The resulting reflection coefficient is quite high, (-0.5 to -0.16 dB) within the band of interest. This is good, as a high reflection coefficient means that almost all power that is incident on the RA surface, is reflected back. In terms of the phase response, the phase shift introduced by the cell was analyzed for an outer ring lengths from 1.1 to 2.7 mm, with steps of 0.1 mm. Figure 4.8 illustrates the S-shaped curve of the introduced phase shift in terms of the outer ring length, for normal field incidence.

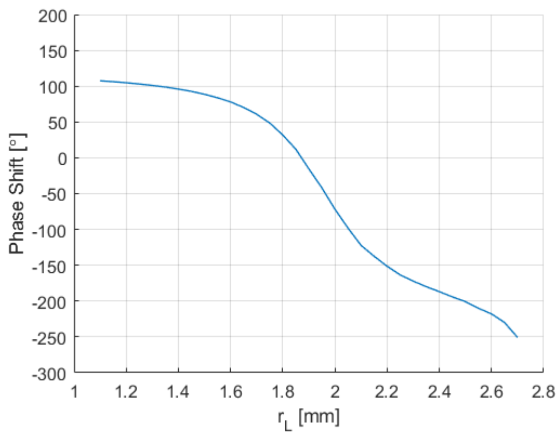

Figure 4.8: Unit cell's reflection coefficient phase for different outer ring side lengths.

The obtained phase shift covers the whole 360° range (-250° to 100°). The dependence of the phase response in terms of incidence angle was also studied. This study is important because in this RA system, the feed is offset, tilted and quite close to the RA surface. Figure 4.9 shows the different phase responses for different incidence angles, ranging from 0° to 60°, which represent the maximum and minimum incidence angles between the feed and the RA surface.

There is a noticeable difference on the S-curves when the incidence angle is higher than 40°. Because of this, the incidence angle will be taken into account when matching a certain outer ring length to a necessary phase shift. This decision of including the incidence angle will not improve the RA antenna's

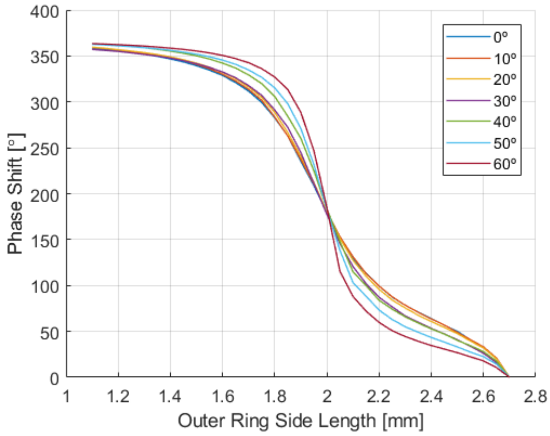

Figure 4.9: Unit cell's reflection coefficient phase for different outer ring side lengths, and different incidence angles.

gain, but it will lower the side lobe levels.

4.5 Reflect Array Full-Wave Simulations

The next step, after designing the unit cells, consists in designing the whole RA surface. The results in figure 4.9, for each incidence angle, consist of discrete values with a step size of 0.1 mm. In order to obtain a continuous function with the phase shift depending on the outer ring length, a polynomial fit of 10th order was used, for each S-curve. It was then possible to assign a specific outer ring length to a necessary phase shift, represented in figure 4.3. Figure 4.10 illustrates the designed RA antenna model.

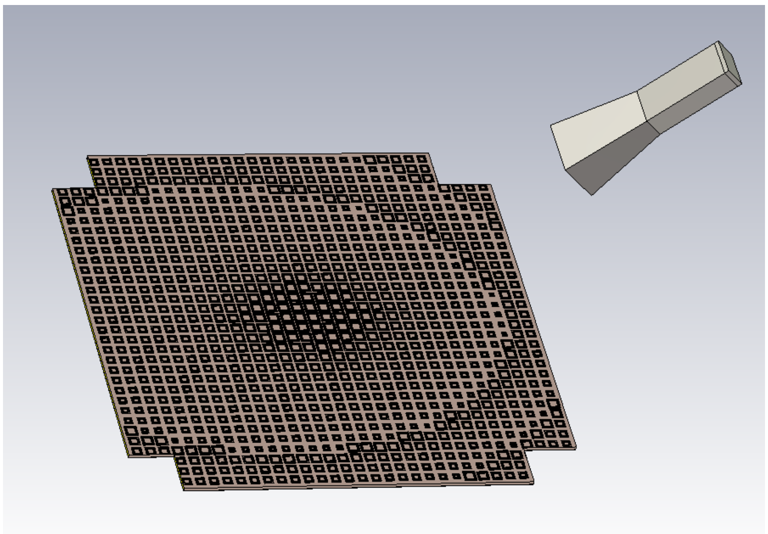

Figure 4.10: 3D model of the designed reflect array antenna, including the reflect array surface and a horn antenna as the feed.

The RA surface consists of 1089 cells like the one in figure 4.6, with changing outer ring lengths. The corners of the 10 x 10 cm^2 RA surface where cut in order to fit into the small 1U CubeSat bottom face, between the structural pillars. In this thesis, a horn antenna was used instead of a planar feed solution. The horn antenna feed has 10.8 dB of gain at 30 GHz. Two simulations were performed with the horn antenna in two orthogonal positions, in order to emulate a circularly polarized feed by post-processing. The horn antenna is not intended to be the feed for this RA system as it is relatively large at these frequencies, which means that it will protrude the 1U CubeSat's bottom face. Despite this, the horn antenna serves perfectly to test the developed RA surface, as it does not change the fundamental concept, nor the validity of the demonstration. Also, the design and fabrication of a planar, circularly polarized, tilted beam feed array, is outside of the scope of this thesis.

The RA antenna was simulated using the time domain solver of CST-MWS. Figure 4.11 shows the simulated farfield results for both rotations of the feed.

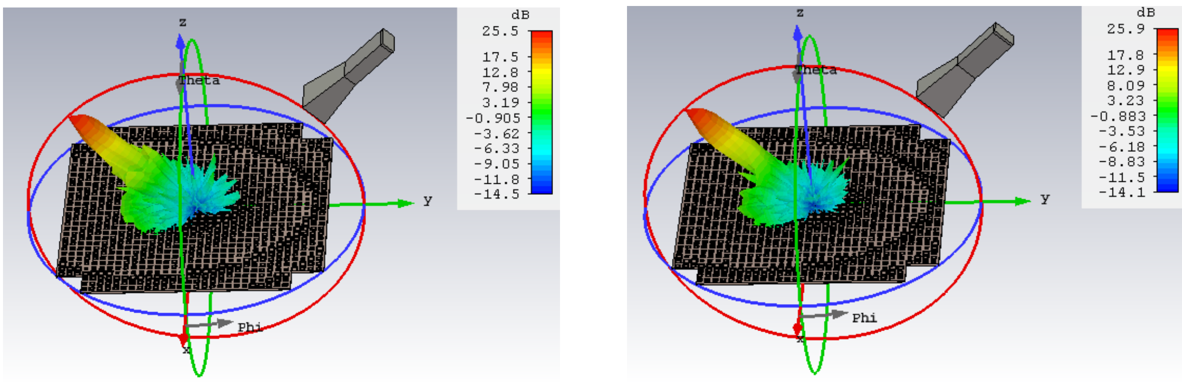

(a) **(b)**

Figure 4.11: Simulated radiation pattern results. (a) Feed in horizontal position. (b) Feed in vertical position.

The gain obtained, using full-wave simulations, matches perfectly with the predicted results using the physical optics tool. In order to represent the radiation pattern in the two orthogonal circular polarized field components, it must be converted from the linear polarized representation. The left circularly polarized component can be defined by

$$L = \frac{E^{\theta\theta} + jE^{\phi\theta} + E^{\phi\phi} - jE^{\theta\phi}}{2}, \tag{4.5}$$

where $E^{\theta\theta}$ and $E^{\phi\theta}$ are the E^{θ} and E^{ϕ} field components with the feed in the position of figure 4.11(a), respectively. $E^{\theta\phi}$ and $E^{\phi\phi}$ are the E^{θ} and E^{ϕ} field components with the feed in the position of figure 4.11(b). Similarly, the right circularly polarized component can be defined by

$$R = \frac{E^{\theta\theta} + jE^{\phi\theta} - E^{\phi\phi} + jE^{\theta\phi}}{2}, \tag{4.6}$$

with all the variables defined above. Figure 4.12 shows a cut for Phi = 90°, of the simulated radiation pattern, represented with circularly polarized components.

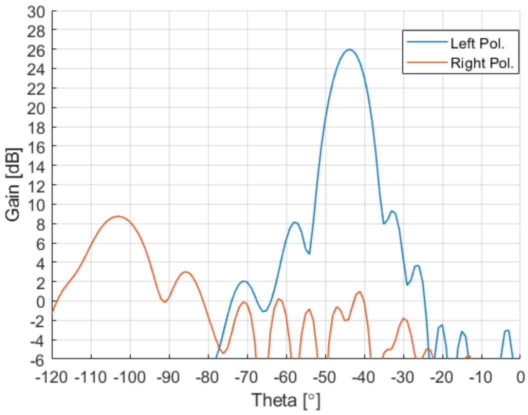

Figure 4.12: Radiation pattern cut for Phi = 90°. The angle Theta = -90° corresponds to normal incidence on the Earth's surface.

The obtained realized gain is 26 dB, at Theta = -44°. The cross-polarization is low at -28 dB, and the side lobe level is -16.7 dB.

4.6 Fabricated Prototype and Measurements

The designed RA antenna was fabricated, and special supports were 3D printed, in order to mount the RA surface and feed to the already built CubeSat structure, the same used in the previous chapter. Figure 4.13 illustrates the fabricated prototype, integrated into the 1U CubeSat structure.

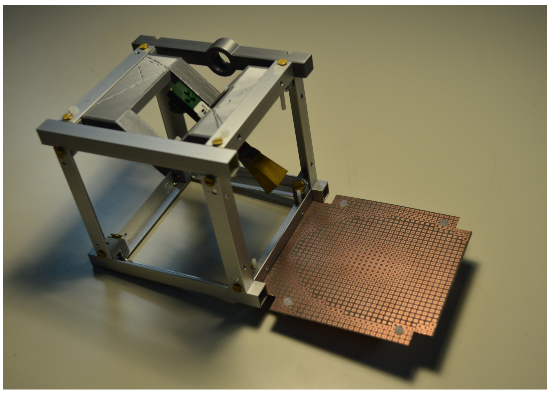

Figure 4.13: Fabricated reflect array antenna, integrated into a CubeSat structure.

For the purpose of this thesis, a fixed mount for the RA array antenna was built, as the development of a deployable mechanism was outside of the scope of this thesis. Despite this, the RA surface was developed with a specific size and geometry so it can, in the future, be integrated into such system.

The fabricated RA antenna's radiation pattern was measured in IT-IST's anechoic chamber number two. Figure 4.14 shows the RA in the anechoic chamber, for the radiation pattern measurements. The results of these measurements are represented in figure 4.15.

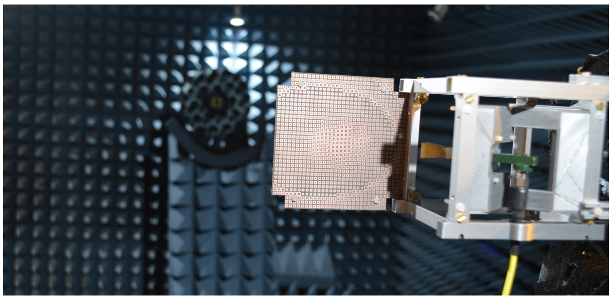

Figure 4.14: RA antenna mounted onto the positioner, in the anechoic chamber.

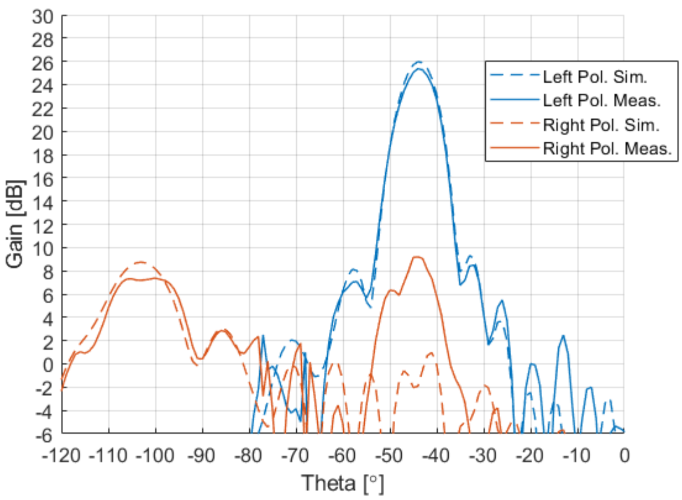

Figure 4.15: Measured and simulated radiation pattern cuts for Phi = 90°.

There is a good agreement between measured and simulated results. The measured gain is 25.4 dB, at Theta = -44°. The measured value is 0.6 dB lower than the simulated one. This is though, a very small difference and can be due to small errors on the anechoic chamber measurement or in the numerical methods. The side lobe level is -16.9 dB and the cross-polarization level is -16.2 dB. The measured cross-polarization level at Theta = -44°, is 11.1 dB higher than the simulated value. This is probably caused by the presence of the CubeSat structure in the measurements. The simulations did not include the structure because this is a very demanding simulation and there was not enough computer power to perform them. From the cross-polarization level, the axial ratio was calculated for different frequencies within the Ka uplink band, and it is represented in figure 4.16.

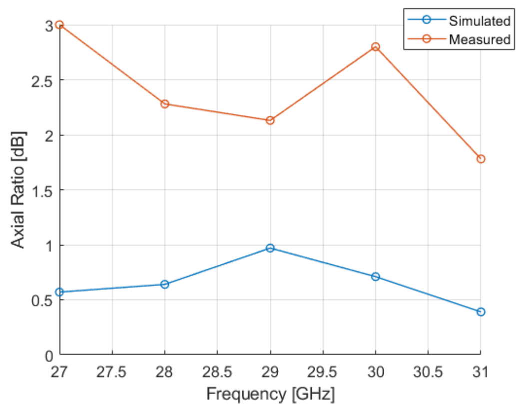

Figure 4.16: Measured and simulated axial ratio for Theta = -45°.

Both in the simulated and measured results, the axial ratio is below 3 dB, for the band of interest. This confirms that the developed RA antenna is indeed circularly polarized. The antenna gain in the frequency band of interest was also measured, and is illustrated in figure 4.17.

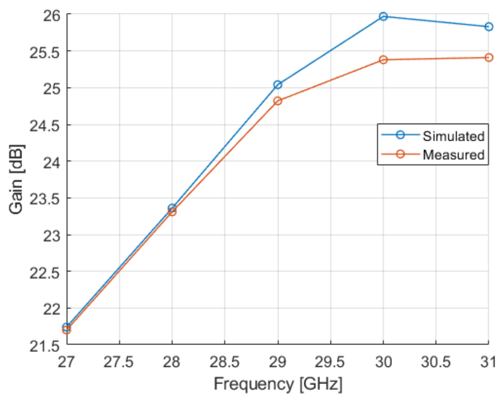

Figure 4.17: Measured and simulated gain for Theta = -45°, in the Ka uplink band.

The -3 dB bandwidth does not cover the whole band, and is from approximately 27.5 GHz to 31 GHz, within the band of interest. However, the fabricated antenna's gain is quite high, and it decays slowly close to the resonance frequency of the unit cells (30 GHz). In order to get a better distribution of antenna gain through the whole Ka uplink band, the cells should have been designed to the center band frequency (29 GHz).

5

Conclusions and Future Work

Contents

Conclusions and Future Work

5.1 Conclusions

There are many challenges an engineer has to face when designing antennas for small satellites. The challenges arise from the harsh conditions experienced in space and the limited space available in these small satellites. CubeSats and their small form factor, only increase these challenges. When designing antennas for CubeSats, especially for low frequencies (L band and below) or for having high gain, compromises need to be taken into account and a trade off analysis between the different antenna solutions needs to be done.

In this thesis, two different antennas for two different CubeSat missions were developed. One for an ADS-B mission for ISTsat-1 and another for fast mobile broadband access applications, in the Ka band. The ADS-B antenna, developed for ISTsat-1, consisted in a circular polarized patch antenna. The antenna was developed following the strict requirements, of limited space, small bandwidth, high enough gain, thermal and mechanically robustness, and designed to work when integrated into the CubeSat. The resulting antenna proved to be a very good solution for this mission, being fabricated in a space rated material, with low outgassing properties. It has a resonance center frequency of 1090 MHz, at 0 °C, and a small bandwidth of 16 MHz. It can operate within its bandwidth, between -25 °C and 25 °C. It is circular polarized, with a low axial ratio of 0.5 dB, at the resonance frequency. Finally, when mounted onto the CubeSat, it maintains a good gain of 3.1 dB, more than enough to receive the airplanes' signals, at 400 km of distance. In the development of this antenna, new tests were performed, such as the antenna performance study under large temperature changes. Also, an extensive study of how an 1U CubeSat structure affects the antenna performance, of a planar antenna mounted on one face, is also presented. Finally, it is presented a novel deployable wire solution that improves the planar antenna's gain.

The developed RA antenna for the Ka band was a novel solution, for this size of CubeSat, and consisted of a circularly polarized solution with high gain, made to be integrated into the small 1U CubeSat structure. The resulting performance of this antenna was very good, considering the small space available. The developed RA antenna is of the deployable type, and it achieved 26 dB of gain, at the resonance frequency of 30 GHz, with a large 3 dB gain bandwidth that covers almost the whole Ka uplink band. These are good results, as it allows for the antenna to be used in HTS, with multiple applications, for the Ka uplink band.

5.2 Future Work

The ADS-B antenna for ISTsat-1 that was developed, fulfills all the strict mission and component requirements, with this in mind the solution is final.

For the Ka band RA antenna, the developed antenna presented very good performance but some improvements can be implemented, to obtain a more solid, complete solution. First, in order to cover the whole Ka uplink band of 27 - 31 GHz, the unit cell design must be adjusted to 29 GHz, instead of the 30 GHz used. Secondly, the development of a planar feed must be done, for the whole RA system to be fully integrated into the CubeSat platform. One possible feed option is to have a circular polarized array of patches, that radiate a tilted beam. That way, the feed can be mounted on the bottom face of the CubeSat, without occupying much space inside the satellite. Finally, in order to be a fully functioning deployable RA for CubeSat applications, the deployment system must be developed. The idea for this is to have two springs, that act as hinges. In the stowed state, the RA surface is folded onto the feed, and held by a pin that fires when a burn wire is activated. Upon deployment the stored strain energy of the springs would deploy the RA surface. Being built on a thin substrate, the light RA surface would need little force for the deployment.

References

[1] CST - Computer Simulation Technology. [Online]. Available: www.cst.com

[2] H. A. Wheeler, "The radiansphere around a small antenna," *Proceedings of the IRE*, vol. 47, no. 8, pp. 1325–1331, Aug 1959.

[3] Sweeting, Martin N. and Underwood, Craig I., "Small satellite engineering and applications," in *Spacecraft systems engineering*. John Wiley & Sons, 2011, pp. 575–605.

[4] Uosat-1 mission page. [Online]. Available: https://www.sstl.co.uk/Missions/UoSAT-1-Launched-1981/UoSAT-1/UoSAT-1-The-Mission

[5] S. Gao, K. Clark, M. Unwin, J. Zackrisson, W. A. Shiroma, J. M. Akagi, K. Maynard, P. Garner, L. Boccia, G. Amendola, G. Massa, C. Underwood, M. Brenchley, M. Pointer, and M. N. Sweeting, "Antennas for modern small satellites," *IEEE Antennas and Propagation Magazine*, vol. 51, no. 4, pp. 40–56, Aug 2009.

[6] L. Alminde, K. Kaas, M. Bisgaard, J. Christiansen, and D. Gerhardt, "Gomx-1 flight experience and air traffic monitoring results," *Small Satellite Conference*, 2014.

[7] A. Mehrparvar, D. Pignatelli, J. Carnahan, R. Munakat, W. Lan, A. Toorian, A. Hutputanasin, and S. Lee, "Cubesat design specification rev 13," *The CubeSat Program, Cal Poly San Luis Obispo, US*, 2014.

[8] Nasa's article. [Online]. Available: https://www.nasa.gov/content/goddard/nasas-science-mission-directorate-cubesat-initiative

[9] W. Blackwell, G. Allen, C. Galbraith, T. Hancock, R. Leslie, I. Osaretin, L. Retherford, M. Scarito, C. Semisch, M. Shields, M. Silver, D. Toher, K. Wight, D. Miller, K. Cahoy, and N. Erickson, "Nanosatellites for earth environmental monitoring: The micromas project," in *2012 12th Specialist Meeting on Microwave Radiometry and Remote Sensing of the Environment (MicroRad)*, March 2012, pp. 1–4.

[10] M. W. Smith, S. Seager, C. M. Pong, J. S. Villaseñor, G. R. Ricker, D. W. Miller, M. E. Knapp, G. T. Farmer, and R. Jensen-Clem, "Exoplanetsat: detecting transiting exoplanets using a low-cost cubesat platform," in *SPIE Astronomical Telescopes + Instrumentation*. International Society for Optics and Photonics, 2010, pp. 773 127–773 127.

[11] A. Marinan, A. Nicholas, and K. Cahoy, "Ad hoc cubesat constellations: Secondary launch coverage and distribution," in *2013 IEEE Aerospace Conference*, March 2013, pp. 1–15.

[12] A. B. Constantine *et al.*, "Antenna theory: analysis and design," *MICROSTRIP ANTENNAS, third edition, John wiley & sons*, 2005.

[13] J. Costantine, Y. Tawk, C. G. Christodoulou, J. Banik, and S. Lane, "Cubesat deployable antenna using bistable composite tape-springs," *IEEE Antennas and Wireless Propagation Letters*, vol. 11, pp. 285–288, 2012.

[14] A. Thurn, S. Huynh, S. Koss, P. Oppenheimer, S. Butcher, J. Schlater, and P. Hagan, "A nichrome burn wire release mechanism for cubesats," in *The 41st Aerospace Mechanisms Symposium*, 2012, pp. 479–488.

[15] A failure analysis of the exocube cubsat. [Online]. Available: http://mstl.atl.calpoly.edu/~bklofas/Presentations/DevelopersWorkshop2016/5_AlexSaunders.pdf

[16] D. Ochoa, K. Hummer, and M. Ciffone, "Deployable helical antenna for nano-satellites," in *Proceedings of the 28th Annual AIAA/USU Conference on Small Satellites*, August 2014, pp. 1–7.

[17] K. Carver and J. Mink, "Microstrip antenna technology," *IEEE Transactions on Antennas and Propagation*, vol. 29, no. 1, pp. 2–24, Jan 1981.

[18] Y. X. Guo, L. Bian, and X. Q. Shi, "Broadband circularly polarized annular-ring microstrip antenna," *IEEE Transactions on Antennas and Propagation*, vol. 57, no. 8, pp. 2474–2477, Aug 2009.

[19] N. Jin, F. Yang, and Y. Rahmat-Samii, "A novel patch antenna with switchable slot (pass): dual-frequency operation with reversed circular polarizations," *IEEE Transactions on Antennas and Propagation*, vol. 54, no. 3, pp. 1031–1034, March 2006.

[20] Y. J. Sung, T. U. Jang, and Y. S. Kim, "A reconfigurable microstrip antenna for switchable polarization," *IEEE Microwave and Wireless Components Letters*, vol. 14, no. 11, pp. 534–536, Nov 2004.

[21] H. Iwasaki, "A circularly polarized small-size microstrip antenna with a cross slot," *IEEE Transactions on Antennas and Propagation*, vol. 44, no. 10, pp. 1399–1401, Oct 1996.

[22] H. Zhang, Y. Q. Li, X. Chen, Y. Q. Fu, and N. C. Yuan, “Design of circular/dual-frequency linear polarization antennas based on the anisotropic complementary split ring resonator,” *IEEE Transactions on Antennas and Propagation*, vol. 57, no. 10, pp. 3352–3355, Oct 2009.

[23] C. G. Kakoyiannis and P. Constantinou, “A compact microstrip antenna with tapered peripheral slits for cubesat rf payloads at 436mhz: Miniaturization techniques, design and numerical results,” in *2008 IEEE International Workshop on Satellite and Space Communications*, Oct 2008, pp. 255–259.

[24] A. Boriskin and R. Sauleau, “Aperture antennas for millimeter and sub-millimeter wave applications,” 2017.

[25] X. Xia, Q. Wu, H. Wang, C. Yu, and W. Hong, “Wideband millimeter-wave microstrip reflectarray using dual-resonance unit cells,” *IEEE Antennas and Wireless Propagation Letters*, vol. 16, pp. 4–7, 2017.

[26] C. Han, C. Rodenbeck, J. Huang, and K. Chang, “A c/ka dual frequency dual layer circularly polarized reflectarray antenna with microstrip ring elements,” *IEEE Transactions on Antennas and Propagation*, vol. 52, no. 11, pp. 2871–2876, Nov 2004.

[27] C. Han, J. Huang, and K. Chang, “A high efficiency offset-fed x/ka-dual-band reflectarray using thin membranes,” *IEEE Transactions on Antennas and Propagation*, vol. 53, no. 9, pp. 2792–2798, Sept 2005.

[28] Radartutorial website. [Online]. Available: http://www.radartutorial.eu/06.antennas/FeedingSystems.en.html

[29] A. H. Abdelrahman, A. Z. Elsherbeni, and F. Yang, “Transmission phase limit of multilayer frequency-selective surfaces for transmitarray designs,” *IEEE Transactions on Antennas and Propagation*, vol. 62, no. 2, pp. 690–697, Feb 2014.

[30] E. B. Lima, S. A. Matos, J. R. Costa, C. A. Fernandes, and N. J. G. Fonseca, “Circular polarization wide-angle beam steering at ka-band by in-plane translation of a plate lens antenna,” *IEEE Transactions on Antennas and Propagation*, vol. 63, no. 12, pp. 5443–5455, Dec 2015.

[31] L. Dussopt, A. Moknache, J. Säily, A. Lamminen, M. Kaunisto, J. Aurinsalo, T. Bateman, and J. Francey, “A v-band switched-beam linearly polarized transmit-array antenna for wireless backhaul applications,” *IEEE Transactions on Antennas and Propagation*, vol. 65, no. 12, pp. 6788–6793, Dec 2017.

[32] S. V. Hum and J. Perruisseau-Carrier, "Reconfigurable reflectarrays and array lenses for dynamic antenna beam control: A review," *IEEE Transactions on Antennas and Propagation*, vol. 62, no. 1, pp. 183–198, 2014.

[33] C. Tienda, M. Younis, P. Lopez-Dekker, and P. Laskowski, "Ka-band reflectarray antenna system for SAR applications," in *Antennas and Propagation (EuCAP), 2014 8th European Conference on*. IEEE, 2014, pp. 1603–1606.

[34] S.-H. Hsu, C. Han, J. Huang, and K. Chang, "An offset linear-array-fed ku/ka dual-band reflectarray for planet cloud/precipitation radar," *IEEE Transactions on Antennas and Propagation*, vol. 55, no. 11, pp. 3114–3122, 2007.

[35] K. K. Karnati, Y. Shen, M. E. Trampler, S. Ebadi, P. F. Wahid, and X. Gong, "A bst-integrated capacitively loaded patch for K_a- and X-band beamsteerable reflectarray antennas in satellite communications," *IEEE Transactions on Antennas and Propagation*, vol. 63, no. 4, pp. 1324–1333, April 2015.

[36] Q. Luo, S. Gao, C. Zhang, D. Zhou, T. Chaloun, W. Menzel, V. Ziegler, and M. Sobhy, "Design and analysis of a reflectarray using slot antenna elements for ka-band satcom," *IEEE Transactions on Antennas and Propagation*, vol. 63, no. 4, pp. 1365–1374, 2015.

[37] R. E. Hodges, M. J. Radway, A. Toorian, D. J. Hoppe, B. Shah, and A. E. Kalman, "Isara - integrated solar array and reflectarray cubesat deployable ka-band antenna," in *2015 IEEE International Symposium on Antennas and Propagation USNC/URSI National Radio Science Meeting*, July 2015, pp. 2141–2142.

[38] W. An, S. Xu, F. Yang, and J. Gao, "A ka-band reflectarray antenna integrated with solar cells," *IEEE Transactions on Antennas and Propagation*, vol. 62, no. 11, pp. 5539–5546, Nov 2014.

[39] T. Chaloun, C. Hillebrand, C. Waldschmidt, and W. Menzel, "Active transmitarray submodule for k/ka band satcom applications," in *Microwave Conference (GeMiC), 2015 German*. IEEE, 2015, pp. 198–201.

[40] C. Huang, W. Pan, X. Ma, B. Zhao, J. Cui, and X. Luo, "Using reconfigurable transmitarray to achieve beam-steering and polarization manipulation applications," *IEEE Transactions on Antennas and Propagation*, vol. 63, no. 11, pp. 4801–4810, 2015.

[41] S. A. Matos, E. B. Lima, J. S. Silva, J. R. Costa, C. A. Fernandes, N. J. G. Fonseca, and J. R. Mosig, "High gain dual-band beam-steering transmit array for satcom terminals at ka-band," *IEEE Transactions on Antennas and Propagation*, vol. 65, no. 7, pp. 3528–3539, July 2017.

[42] A. Clemente, L. Dussopt, R. Sauleau, P. Potier, and P. Pouliguen, “Focal distance reduction of transmit-array antennas using multiple feeds,” *IEEE Antennas and Wireless Propagation Letters*, vol. 11, pp. 1311–1314, 2012.

[43] J. G. Nicholls and S. V. Hum, “Full-space electronic beam-steering transmitarray with integrated leaky-wave feed,” *IEEE Transactions on Antennas and Propagation*, vol. 64, no. 8, pp. 3410–3422, 2016.

[44] C. Pfeiffer and A. Grbic, “Planar lens antennas of subwavelength thickness: Collimating leaky-waves with metasurfaces,” *IEEE Transactions on Antennas and Propagation*, vol. 63, no. 7, pp. 3248–3253, 2015.

[45] A. Designation, “Standard test method for total mass loss and collected volatile condensable materials from outgassing in a vacuum environment,” *E595-93*, 1993.

[46] M. M. Finckenor, “Materials for spacecraft. chapter 6,” 2016.

[47] A. Lepore Jr, H. Wong, S. L. Marr, and L. J. Amore, “Rf-transparent antenna sunshield membrane,” Dec. 13 1994, uS Patent 5,373,305.

[48] R. Van Der Pryt and R. Vincent, “A simulation of the reception of automatic dependent surveillance-broadcast signals in low earth orbit,” *International Journal of Navigation and Observation*, vol. 2015, 2015.

[49] J. M. Felício, C. A. Fernandes, and J. R. Costa, “Complex permittivity and anisotropy measurement of 3d-printed pla at microwaves and millimeter-waves,” in *Applied Electromagnetics and Communications (ICECOM), 2016 22nd International Conference on*. IEEE, 2016, pp. 1–6.

[50] Amphenol website. [Online]. Available: https://www.amphenolrf.com/908-24100.html

[51] uavionix website. [Online]. Available: https://uavionix.com/products/pingrx/

[52] Ardupilot website. [Online]. Available: https://github.com/ArduPilot/mavlink

[53] Mavlink source code. [Online]. Available: https://github.com/ArduPilot/mavlink

[54] Flightradar24 website. [Online]. Available: https://www.flightradar24.com

[55] C. A. Fernandes, “Kh3d_near. User’s manual, Version 0.2g,” *Instituto de Telecomunicações - IST*, Feb 2018.